

Modeling the Expected Performance of the REgolith X-ray Imaging Spectrometer (REXIS)

Niraj K. Inamdar^{a*}, Richard P. Binzel^a, Jae Sub Hong^b, Branden Allen^b,
Jonathan Grindlay^b, Rebecca A. Masterson^c

^aMassachusetts Institute of Technology, Department of Earth, Atmospheric
and Planetary Sciences, Cambridge, MA

^bHarvard-Smithsonian Center for Astrophysics, Cambridge, MA

^cMassachusetts Institute of Technology, Space Systems Laboratory, Cambridge, MA

Abstract

OSIRIS-REx is the third spacecraft in the NASA New Frontiers Program and is planned for launch in 2016. OSIRIS-REx will orbit the near-Earth asteroid (101955) Bennu, characterize it, and return a sample of the asteroid's regolith back to Earth. The Regolith X-ray Imaging Spectrometer (REXIS) is an instrument on OSIRIS-REx designed and built by students at MIT and Harvard. The purpose of REXIS is to collect and image sun-induced fluorescent X-rays emitted by Bennu, thereby providing spectroscopic information related to the elemental makeup of the asteroid regolith and the distribution of features over its surface.

Telescopic reflectance spectra suggest a CI or CM chondrite analog meteorite class for Bennu, where this primitive nature strongly motivates its study. A number of factors, however, will influence the generation, measurement, and interpretation of the X-ray spectra measured by REXIS. These include: the compositional nature and heterogeneity of Bennu, the time-variable Solar state, X-ray detector characteristics, and geometric parameters for the observations.

In this paper, we will explore how these variables influence the precision to which REXIS can measure Bennu's surface composition. By modeling the aforementioned factors, we place bounds on the expected performance of REXIS and its ability to ultimately place Bennu in an analog meteorite class.

1. Introduction

In 2016, NASA is scheduled to launch OSIRIS-REx (“Origins Spectral Interpretation Resource Identification Security Regolith Explorer”), a mission whose goal is to characterize and ultimately return a sample of the near-Earth asteroid (101955) Bennu (formerly 1999 RQ₃₆ and hereafter Bennu)¹. Bennu was chosen as the target asteroid for OSIRIS-REx for several reasons. Spectral similarities in different near-infrared bands to B-type asteroids 24 Themis and 2 Pallas raise the intriguing possibility that Bennu is a transitional object between the two. Furthermore, Bennu's reflectance spectra suggest that it may be related to a CI or CM carbonaceous chondrite analog meteorite class². Carbonaceous chondrites are believed to be amongst the most primitive material in the Solar System, undifferentiated and with refractory elemental abundances very similar to the Sun's. The discovery of water on the surface of 24 Themis provides additional scientific motivation for studying Bennu.

Bennu belongs to a class of asteroids known as near-Earth asteroids (NEA). Its semimajor axis is roughly 1 AU, and its orbit crosses Earth's³. While this makes Bennu a particularly accessible target for exploration, it also makes Bennu a non-negligible impact risk to Earth. Calculations of Bennu's orbital elements suggest an impact probability of $\sim 10^{-4} - 10^{-3}$ by the year 2182,

*Corresponding author. Email: inamdar@mit.edu

which coupled with its relatively large size (mean radius ~ 250 m) makes Bennu one of the most hazardous asteroids known⁴.

Taken together, these unique features make Bennu an attractive target for future study. In order to better characterize Bennu’s composition and physical state, OSIRIS-REx is equipped with a suite of instruments, amongst which is REXIS. REXIS, a student experiment aboard OSIRIS-REx, is an X-ray imaging spectrometer (“**RE**gololith **X**-ray **I**maging **S**pectrometer”) whose purpose is to reconstruct elemental abundance ratios of Bennu’s regolith by measuring X-rays fluoresced by Bennu in response to Solar X-rays (Fig. 1)^{5,6}. More details regarding REXIS’s systems-level organization and operation can be found in Jones, *et al.*⁶.

1.1. Description of REXIS

REXIS is comprised by two distinct, complementary instruments. The first is the primary spectrometer. Measuring approximately 37 cm high and 20 cm wide, it is mounted on the main instrument deck of OSIRIS-REx and houses 4 charged coupled devices (CCDs) that measure X-rays emitted by the Bennu’s regolith (Fig. 2). REXIS images X-rays by means of a coded aperture mask mounted atop the spectrometer tower. The X-ray shadow pattern cast by the mask on the detector plane and knowledge of the mask pattern allows for a reprojection of the measured X-rays back onto the asteroid, so that localized enhancements in the X-ray signal on roughly 50 m scales can be identified on Bennu’s surface. During the mission cruise phase, a radiation cover protects the CCDs from bombardment by nonionizing radiation (such as Solar protons) that can create charge traps in the CCDs and subsequently degrade the detector resolution⁷. This radiation cover is opened prior to calibration and asteroid observations (see below).

REXIS will observe Bennu for an overall observation period of ~ 400 hours. During this time, OSIRIS-REx will be in a roughly circular orbit along the asteroid’s terminator with respect to the Sun and about 1 km from the asteroid barycenter. REXIS will also collect calibration data. Since OSIRIS-REx orbits Bennu at approximately 1 km from the asteroid barycenter, and thus has a field of view that extends beyond the asteroid limb, cosmic sources of X-rays are a potential source of noise. Therefore, prior to asteroid observation, REXIS will observe the cosmic X-ray background (CXB) for a total of 3 hours. Furthermore, a period of 112 hours will be devoted to internal calibration to determine sources of X-ray noise intrinsic to the instrument itself. Throughout the operational lifetime of REXIS, a set of internal ⁵⁵Fe radiation sources (which decay via electron capture to ⁵⁵Mn with a primary intensity centered at 5.89 keV) will be used to calibrate the CCD gain.

The asteroid X-ray spectrum measured by REXIS depends on both the elemental abundances of the asteroid regolith and the Solar state at the time of measurement. In order to remove this degeneracy, a secondary instrument is required to measure Solar activity. The Solar X-ray Monitor (SXM), which is mounted on the Sun-facing side of REXIS, measures Solar activity and hence performs this function. The SXM contains a silicon drift diode (SDD) detecting element manufactured by Amptek, and generates a histogram of the Solar X-ray spectrum over each 32 s observational cadence. The Solar X-rays collected by the SXM allow for a time-varying reconstruction of the Solar state, so that, in principle, the only unknowns during interpretation of the asteroid spectrum are the regolith elemental abundances. The elemental abundances that we infer from the collected spectra are then used to map Bennu back to an analog meteorite class.

During the REXIS observation period, X-rays emitted by Bennu are collected on board by CCDs (CCID-41s manufactured by MIT Lincoln Laboratory). The spectra that are generated from these data are then used to interpret the elemental abundance makeup of the asteroid. The baseline CCD data flow in a single stream, and REXIS data are processed in three distinct “modes”: (Fig. 3). These are:

Spectral Mode. Only the overall accumulation of spectral CCD data over the instrument’s observational period are considered. No attempt is made at producing local elemental abundance or abundance ratio maps. Instead, the data are used to determine the average composition of the asteroid from the spectral data collected in order to correlate Bennu to a meteorite class of similar composition.

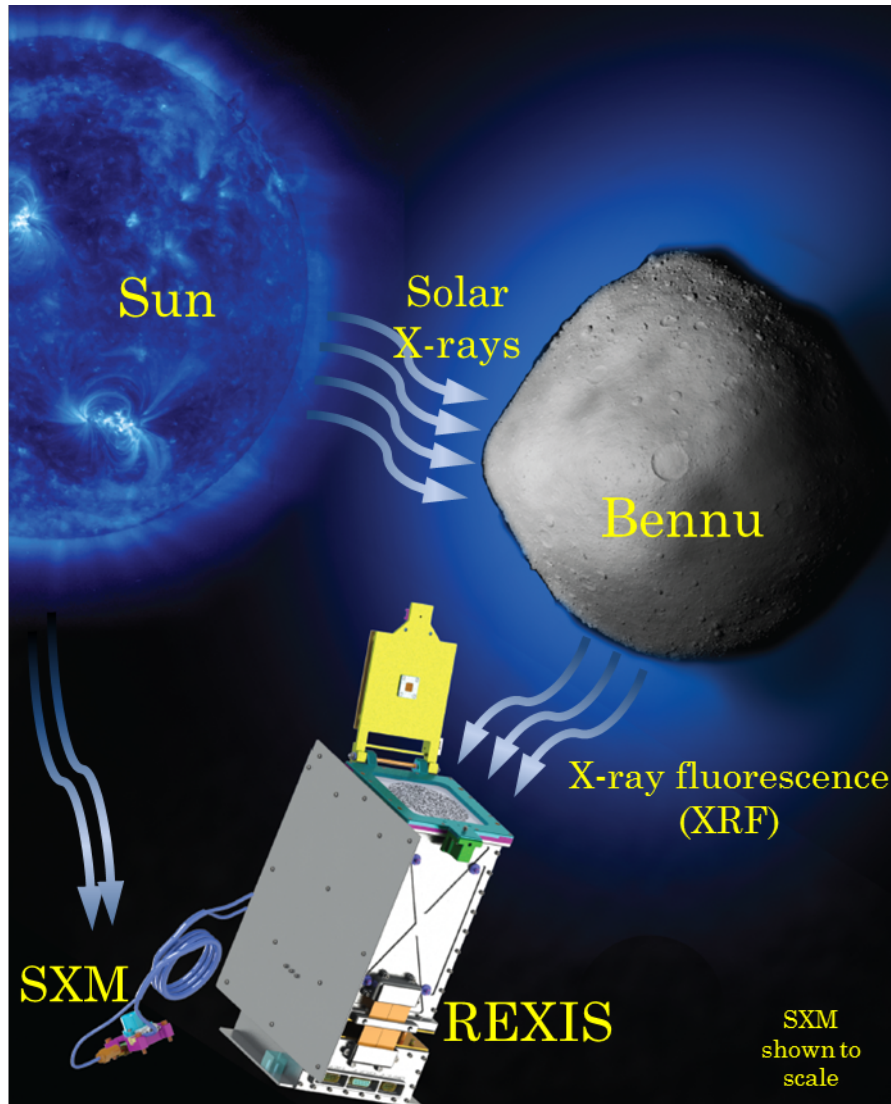


Figure 1: REXIS principle of operation demonstrated schematically. Except for the Solar X-ray Monitor, which is shown to scale relative to REXIS, the rest of the figure is not to scale. X-rays from the Sun impinge the regolith of Bennu, giving rise to X-ray fluorescence. These X-rays enter REXIS, where they are collected by CCDs. The radiation cover (shown in yellow) serves as a shade to prevent Solar radiation from entering REXIS. At the same time, the Solar X-ray Monitor (SXM), which is mounted on a different surface of OSIRIS-REx, collects Solar X-rays directly in order to understand the time variance of the Solar X-ray spectrum. The OSIRIS-REx spacecraft is not shown.

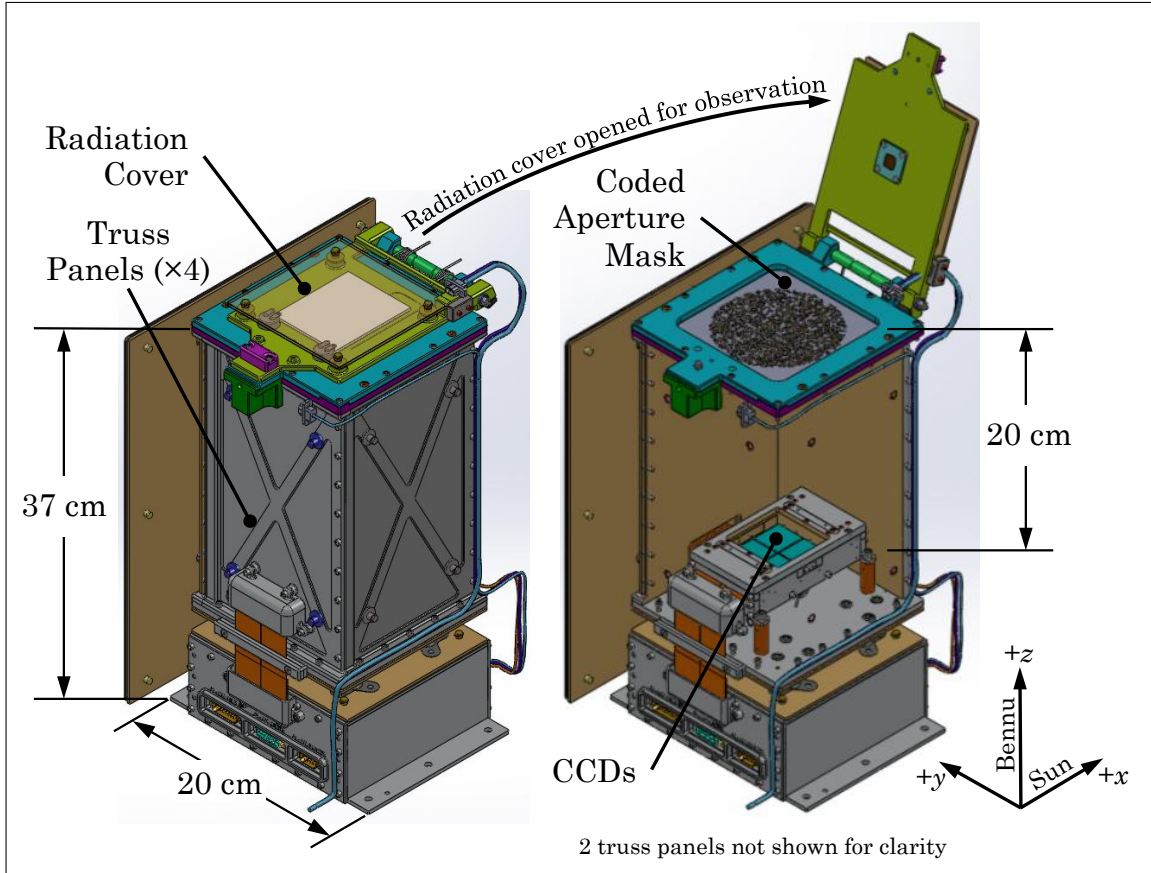


Figure 2: REXIS geometry. On the left, we show the instrument while it is in its stowed position, with the radiation cover closed in order to protect the CCDs from radiation damage. On the right, we show the instrument in its observing state, with the radiation cover opened to allow the CCDs to collect X-rays. The coded aperture mask is mounded above the truss structure and allows for fine angular resolution detection of local elemental abundances in Imaging Mode. In Collimator Mode, however, the telescopic “focal length” of 20 cm and the diameter of the coded aperture mask (9.84 cm) provide the coarse angular resolution. In Spectral Mode, which we focus on in this paper, the surface area of the CCDs, the diameter of the coded aperture mask, and the focal length drive the instrument grasp (see Sec. 2.2.3).

Collimator Mode. Coarse spatially resolved measurements of elemental abundances on the surface of Bennu are carried out in collimator mode using time resolved spectral measurements combined with the instrument attitude history and field of view (FOV) response function. The FOV response function is uniquely determined by the instrument focal length as well as the diameter and open fraction of the coded aperture mask.

Imaging Mode. Higher spatial resolution spectral features on the asteroid surface are identified by applying coded aperture imaging⁸. In each time step, the data are the same as in collimator mode, though the distribution of counts on the detector plane is reprojected (using the known mask pattern and an appropriate deconvolution technique) onto the asteroid surface. Science processing modes occur on the ground. Here, we are concerned with the performance of REXIS in Spectral Mode; discussion of REXIS's performance in imaging and collimator mode may be found in Allen, *et al.*⁵

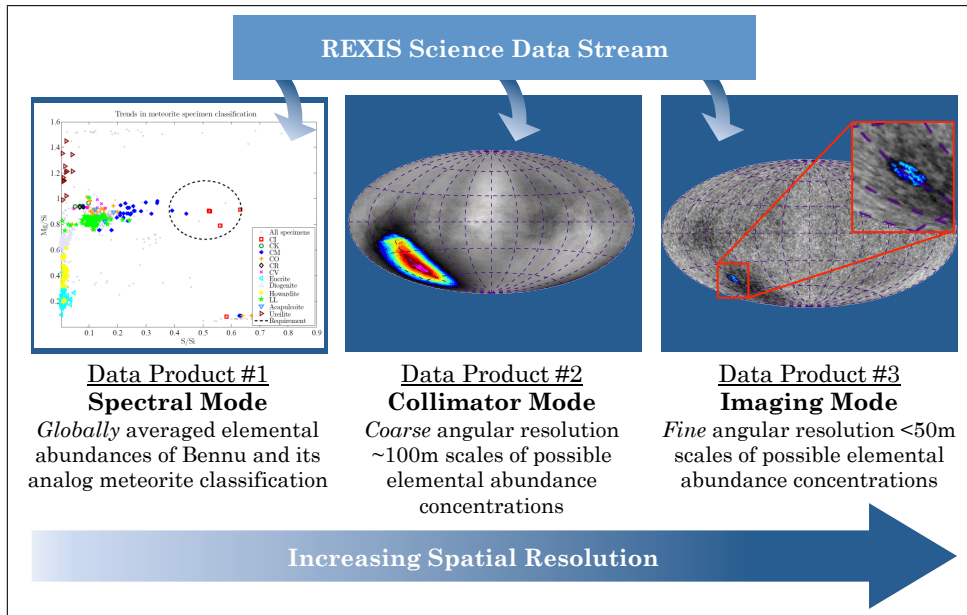


Figure 3: REXIS data processing modes. All data processing modes rely on the same data set, indicated schematically above. In this paper, we focus on modeling the baseline performance of Spectral Mode, in which the globally-averaged spectrum of Bennu is used without regard to spatial variations of spectral features on the surface in order to place Bennu within an analog meteorite class.

1.2. Placing Bennu Within an Analog Meteorite Class

One of the goals of REXIS is to place Bennu within an analog meteorite class. Meteorites of similar class can often be grouped based on chemical or isotopic similarity. In particular, it has been recognized that major chondritic and achondritic meteorite groups can be distinguished on the basis of elemental abundance ratios, as can various subchondritic types⁹. In Fig. 4, we show how various meteorite classes can be grouped on the basis of elemental abundance ratios of Fe/Si, Mg/Si, and S/Si. REXIS therefore collects X-rays between energies of 0.5 and 7.5 keV, within which prominent Fe, Mg, S, and Si emission features are found. The particular X-ray energies associated with these elements are summarized in Table 1. Consistent with the measurement of the X-ray signatures of these elements, REXIS has two high-level requirements associated with its performance in Spectral Mode. These are

- REX-3: REXIS shall be able to measure the global ratios of Mg/Si, Fe/Si, and S/Si of Bennu within 25% for that of a CI chondrite illuminated by a 4 MK, A3.3 Sun.

- REX-6: REXIS shall meet performance requirements given no less than 420 hours of observation time of Benu.

The first reflects the fact that REXIS must measure the stated elemental abundance ratios to within 25% those of a typical CI chondrite during the quiet Sun. 25% error is sufficient to distinguish between achondritic and chondritic types, as well as amongst various chondrite types, as indicated in Fig. 4 by the dashed line ellipses. The second requirement reflects the fact that REXIS must attain its science objectives within its allotted observation period.

Table 1: Summary of lines of interest and their energies¹⁰. In some cases, due to the close proximity of spectral features to one another, they are combined with one another in the analysis below.

Line Designation	Energy center [eV]	Notes
Fe-L α	705.0	Due to proximity, is combined with Fe-L β
Fe-L β	718.5	Due to proximity, is combined with Fe-L α
Mg-K α_1 /K α_2	1,253.60	Due to proximity, is combined with Mg-K β
Mg-K β	1,302.2	Due to proximity, is combined with Mg-K α_1 /K α_2
Si-K α_1 /K α_2	1,739.98/1,739.38	—
S-K α_1 /K α_2	2,307.84/2,306.64	—

Our purpose in this work is to determine, for a given asteroid regolith composition, Solar state, and instrument characteristics, the spectrum that we expect to collect from the asteroid and the impact of data collection and processing on the eventual reconstruction of the hypothetical elemental abundances of Benu. We model the expected performance of REXIS in its Spectral Mode and place bounds on its ability to place Benu within an analog meteorite class. We will accomplish this in several steps. First, we model the ideal X-ray spectra that we expect to be generated by Benu and the Sun. We then model the instrument response for both the spectrometer and the SXM, accounting for factors such as total throughput, detector active area, quantum efficiency, and spectral broadening. We then model the data processing. Here, we combine the instrument response-convolved spectra from both Benu and the Sun to determine how well we can reconstruct Benu’s elemental abundances and place the asteroid within an analog meteorite class. We show that REXIS can accomplish its required objectives with sufficient margin.

2. Methodology

Our overall methodology in simulating the expected performance of REXIS is summarized in Fig. 5. Our basic procedure is to first simulate physical observables—in our case, asteroid and Solar spectra—under expected conditions. We then simulate the process of data collection for both the spectrometer and the SXM. Finally, we simulate the interpretation of the data and assess our ability to reconstruct the original observables using our processed data. In order to assess our expected performance, throughout the entire modeling process, we keep track of all simulated quantities, including those that would be unknowns during the mission lifetime, such as the actual Solar and asteroid spectrum.

2.1. Simulating Observables

The baseline observables for the spectrometer and the SXM are the asteroid and Solar X-ray spectra, respectively. For the discussion that follows, we denote the asteroid spectrum $I_B(E)$ and the Solar spectrum $I_\odot(E)$. The cosmic X-ray background spectrum, which we must also consider, is denoted $I_{\text{CXB}}(E)$. In each case, the spectrum is a function of energy E and has units of photons/cm²/s/Sr/keV. Based on ground observations, the expected asteroid spectrum I_B is that from a CI-like asteroid regolith. Since the OSIRIS-REx mission occurs during the Solar minimum, the expected Solar spectrum is that from a quiet Sun.

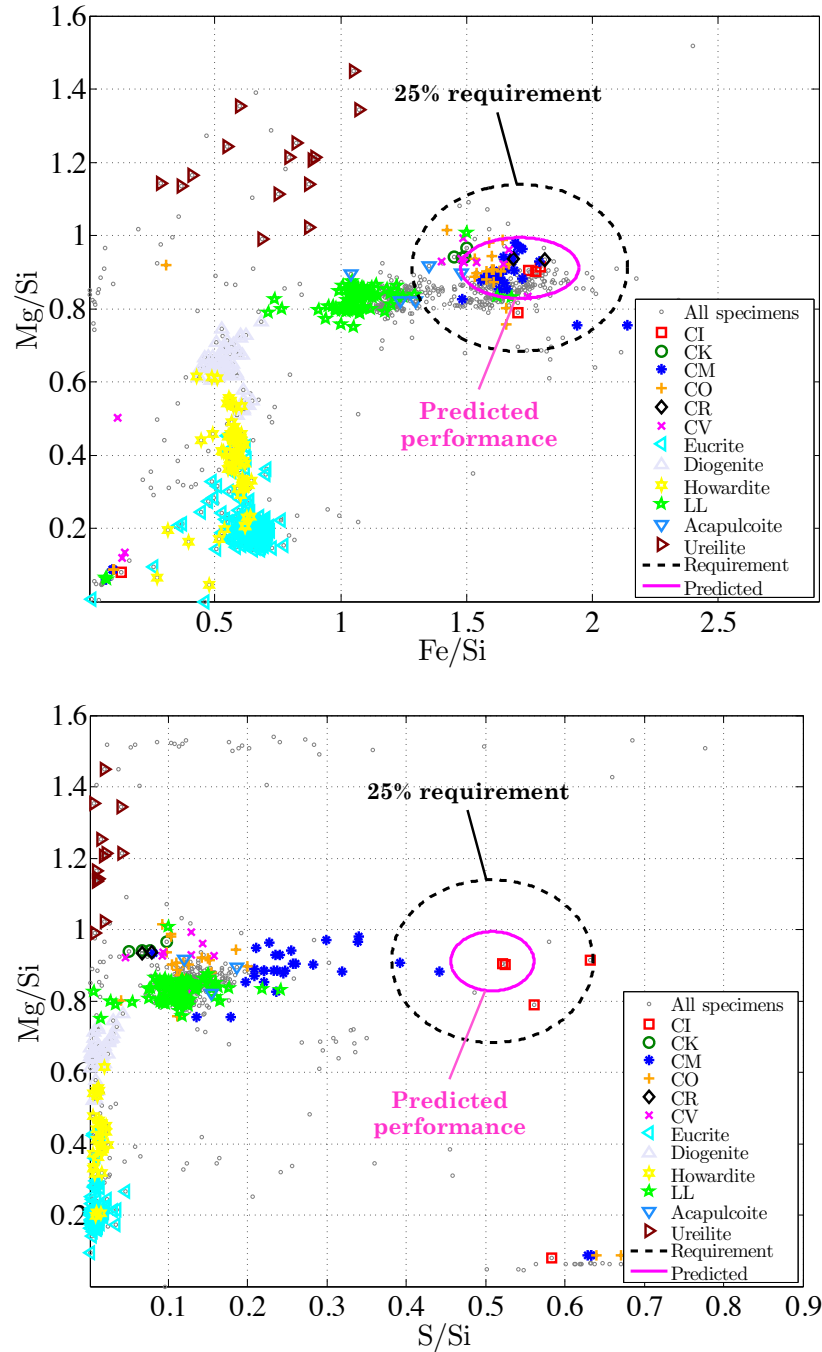


Figure 4: Trends in meteorite classification as a function of elemental abundance ratios. In the upper panel, we see how achondritic and chondritic meteorite specimens can be distinguished on the basis of their Mg/Si and Fe/Si elemental abundance ratios⁹. To differentiate between various chondrite subtypes, we rely on the Mg/Si and S/Si ratios (lower panel). In both panels, we show the REXIS requirement of 25% error centered around a CI chondrite-like baseline. The expected REXIS performance under nominal conditions is indicated in the magenta ellipses. These error ellipses represent systematic error; further consideration of statistical error places the confidence in these calculations of systematic error at 3.5σ (see Sec. 3). Composition data for meteorites are from Nittler, *et al.*⁹.

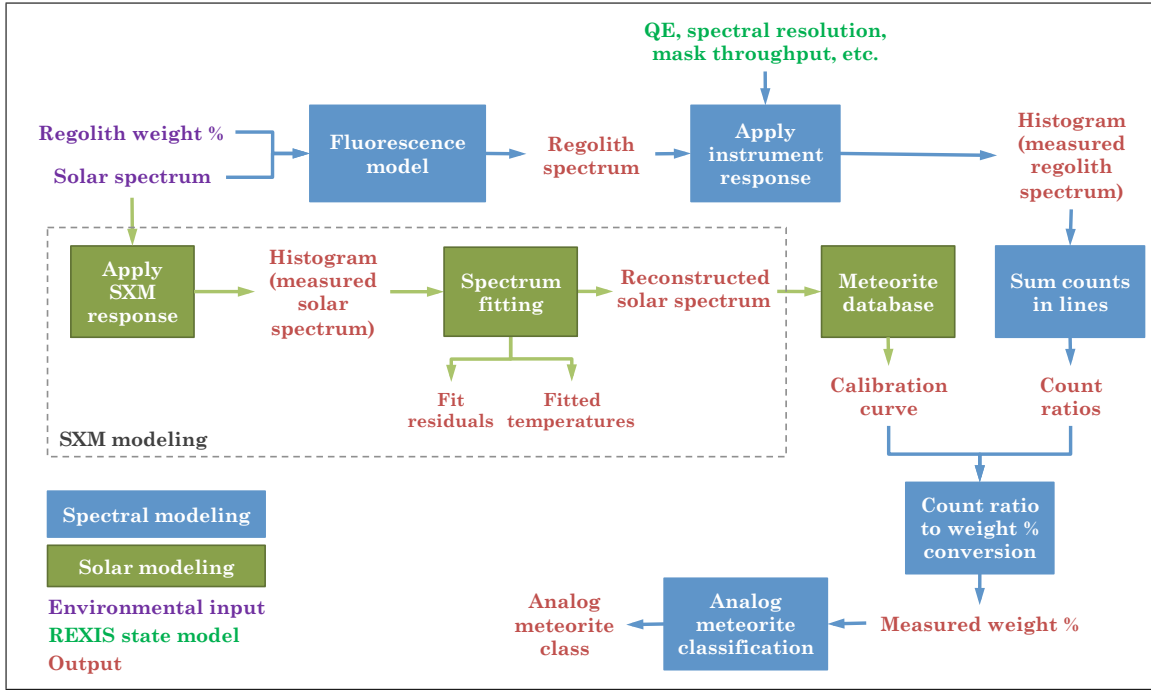


Figure 5: Spectral mode simulation pipeline. In this flow diagram, we indicate the various processes contained in our simulations. The primary inputs may be broadly characterized as environmental inputs (regolith composition, Solar spectrum; purple text) and REXIS state inputs, which includes geometric factors and detector characteristics accounting for the overall instrument response function (green text). Environmental inputs are used to create a synthetic regolith spectrum, to which the instrument response is then applied. Data processing is then simulated. In the SXM simulation, the “actual”, differential emission measure-integrated quiet Solar spectrum is convolved with the SXM response function. We use the resulting histogram, which simulates the actual SXM data product, to reconstruct a best fit isothermal Solar spectrum. The best fit Solar spectrum, which is not detector response-convolved, is then used to generate calibration curves using a meteorite database. These calibration curves map observed photon count ratios to asteroid regolith weight ratios, which we then use to identify Bennu amongst analog meteorite classes.

2.1.1. Asteroid Spectrum

Asteroid spectra are calculated using the standard fluorescence equation for the intensity of the fluorescent lines¹¹. We also include contributions from coherent scattering.* The contribution from incoherent scattering is at least an order of magnitude less than that from coherent scattering and is ignored here¹⁴. We assume the asteroid, which is modeled as a sphere of radius 280 m, is viewed in a circular terminator orbit 1 km from the asteroid center. From the point of view of REXIS, half of the asteroid is illuminated while the other half is dark. Furthermore, the asteroid is not uniformly bright on its Sun-facing side, and the energy-integrated flux peaks at a point offset from the asteroid nadir. The effect of these angles is taken into account when generating the asteroid spectrum (for more details, see Appendix A). The asteroid spectrum itself is a function of the Solar spectrum. It is also, to a much lesser extent, a function of the CXB, which is significantly lower in intensity than the incident Solar radiation, and which is only effective at inducing fluorescence at energies much higher than we are concerned with. In generating $I_B(E)$, we use $I_\odot(E)$, as discussed below in Sec. 2.1.2.

2.1.2. Solar Spectrum

We calculate Solar X-ray spectra $I_\odot(E)$ using the CHIANTI atomic database^{15,16} and SolarSoftWare package¹⁷. The Solar spectrum is that generated by the Solar corona, the primary source of X-rays from the Sun. Since REXIS will be observing Bennu during the Solar minimum, we model the expected Solar spectrum by using the quiet Sun differential emission measure (DEM) derived from the quiet Sun data of Dupree, *et al.*¹⁸ and elemental abundances of Meyer^{19,20}.

The DEM is a quantity that encodes the plasma temperature dependence of the contribution function and hence intensity of the radiation^{14,21,22}. The DEM can be derived from observations, and for the quiet Sun it tends to peak at a single temperature (in the range of about 3 – 6 MK), so that to first order, the Solar corona can be approximated as comprising an isothermal plasma. In general, however, the actual Solar X-ray spectrum will require an integration of the DEM over all temperatures present in the plasma along the observer’s line of sight (see Appendix B). For higher coronal temperatures, access to higher energy states leads to a so-called hardening of the Solar spectrum¹⁴, an effect which is most pronounced during a Solar flare. In this case, the DEM peaks at more than one temperature. Since we expect the majority of our observations to take place while the Sun is relatively inactive, during data processing, we take advantage of the fact that the corona can be approximated as isothermal (for more details, see Appendix B). Finally, we note that the Solar X-ray spectrum depends on the elemental abundances of the Solar corona, for which several models are available¹⁴. However, our results are relatively insensitive to the coronal elemental abundance model employed.

2.1.3. CXB Spectrum

The CXB spectrum that we use in our models is calculated following Lumb, *et al.*²³. In this model, $I_{\text{CXB}}(E)$ is calculated by assuming that the CXB comprises two optically thin components²⁴ and a power law component²⁵. In general, the CXB flux becomes comparable to the asteroid flux at ~ 2 keV, near the S-K complex (see Fig. 6). Measurement of sulfur is critical, since it enables us to differentiate amongst different chondritic varieties (Fig. 4). Hence, we ultimately find that measurement of the S/Si ratio is most sensitive to this particular source of noise and requires the longest amount of measurement time to achieve statistical significance (see Sec. 3.2).

*All X-ray data, including fluorescent line energies, fluorescence yields, jump ratios, relative intensities, photoabsorption cross sections, and scattering cross sections are derived from the compilations of Elam, *et al.*¹² and Kissel¹³. The Kissel scattering cross section data may be found at the following URLs:

- http://ftp.esrf.eu/pub/scisoft/xop2.3/DabaxFiles/f0_rf_Kissel.dat
- http://ftp.esrf.eu/pub/scisoft/xop2.3/DabaxFiles/f0_mf_Kissel.dat
- http://ftp.esrf.eu/pub/scisoft/xop2.3/DabaxFiles/f1f2_asf_Kissel.dat
- http://ftp.esrf.eu/pub/scisoft/xop2.3/DabaxFiles/f0_EPDL97.dat

2.1.4. Internal Background

Fluorescence from the REXIS instrument itself can be present in the signal we measure. Incident X-rays primarily from Bennu (but also from the CXB) can strike the inner portions of the instrument and induce fluorescence. Ideally, a ray-tracing simulation would be carried out to determine the extent of this internal noise. For our work, however, we use data from the Chandra ACIS instrument that has been suitably scaled down to match the detector area of the REXIS CCDs²⁶. A comparison of Bennu’s spectrum with that of the CXB and the internal background is shown in Fig. 6.

2.2. Instrument Response

The next step after simulating the observables is to estimate how these will convolve with the instrument response. Thus we simulate the data collection process by applying the instrument response for both the spectrometer and the SXM to our model spectrum. Inputs into the instrument response models include (along with the symbols that we use to denote each):

- Observation time, T_{obs}
- Coded aperture mask throughput, F (spectrometer only)
- Grasp, $G = A_E \Omega$
 - Effective detector area, A_E
 - Solid angle subtended by source with respect to detector, Ω
- Detector quantum efficiency, $Q(E)$ (a function of energy E)
- Detector histogram bin width, ΔE
- Gain drift
- Detector spectral resolution, FWHM

In all cases where we are evaluating our results, we assume our measurements are well described within the realm of Poisson statistics. The origin of the values used for each of these inputs varies. In sections below, we detail how each of these inputs is derived for our simulations. After the asteroid and Solar spectra have been convolved with the detector response functions, the basic output for each will be a histogram of photon counts as a function of energy. In Table 2, we summarize some of the major observational inputs into our simulations, while others are given in the text that follows.

Table 2: Observational inputs for spectrometer instrument response.

Parameter	Value
Open fraction	40.5%
Histogram binning ΔE [eV/bin]	~ 15
Gain drift [eV]	± 15
Total observation time T_{obs}	423 hours
CXB calibration period T_{CXB}	3 hours
Internal background calibration period T_{int}	112 hours
Solar state	Quiet Sun
Regolith composition	\sim CI chondritic

2.2.1. Observation Time

The observation time, T_{obs} , for the spectrometer is taken to be 423 hours. For the SXM, Solar spectra are recorded as histograms in 32 s intervals, roughly the time scale over which the Solar state can vary substantially. Time T_{CXB} and T_{int} is also allocated for CXB and internal calibration, respectively (see Sec. 2.3.1).

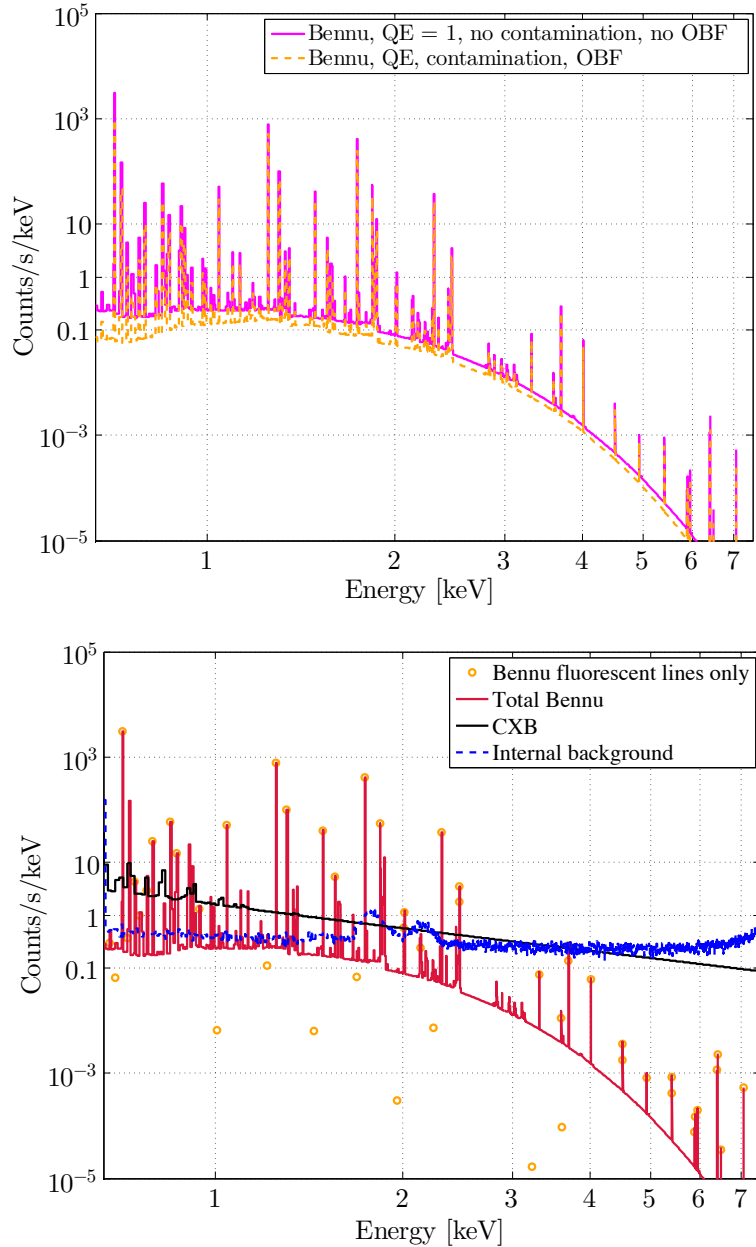


Figure 6: Comparison of spectra of interest at an early stage of our model development. On the left panel, we show our preliminary model of Bennu’s spectrum as emitted directly from the asteroid (solid magenta line). We also show Bennu’s spectrum after detector quantum efficiency, molecular contamination, and the optical blocking filter (OBF; Fig. 7) are taken into account. On the right panel, we show Bennu’s spectrum compared to sources of noise. Fluorescent lines from Bennu are shown as orange markers, while the complete Bennu spectrum, including scattering, is shown in solid red. The cosmic X-ray background (CXB) is shown in black, while internal noise (due to fluorescence from the instrument itself) is shown with the dotted blue line. The Si-K complex from Bennu, which is the prominent set of lines between 2 and 3 keV, is most strongly subject to the effects of noise. Internal background has been scaled from Chandra data²⁶. This model does not include oxygen as it falls just below our model cut-off.

2.2.2. Coded Aperture Mask Throughput

The overall throughput of the instrument depends on the open fraction of the coded aperture mask (the fraction of open mask pixels to total mask pixels). For REXIS, nominally half of the coded aperture pixels are open. However, the presence of a structural grid network to support the closed pixels reduces the throughput further. Since the grid width is 10% of the nominal pixel spacing, the count rate of photons incident on the REXIS detectors will be reduced by a factor $F = 0.5 \times (1 - 0.1)^2 = 0.405$ due to the presence of the coded aperture mask.

2.2.3. Grasp

The grasp G , which has units of cm^2Sr , is the quantity that encodes the solid angle Ω subtended by the target with respect to the detector, and the averaged detector geometric area A_E that sees the target; detector efficiency is not accounted for in this term. The detector area does not comprise a single point, and since the field of view is not a simple cone, G must in general be calculated numerically. We calculate G for the CCDs using custom ray tracing routines in MATLAB and IDL. Since portions of the detector area can see the CXB that extends beyond the limb of the asteroid during observation, we keep track of this as well during our calculations[†]. In Table 3, we summarize G for the CCDs, including individual contributions from Bennu and the CXB.

For the SXM, we assume that the solid angle subtended by the Sun is given by that for a distant source, $\pi (R_\odot/1 \text{ AU})^2$ where R_\odot is the Sun’s radius. Since the Sun is located at such a distance that its incident rays can be treated as parallel, and since there are no structural elements driving the SXM viewing geometry substantially, we calculate G for the SXM by simply multiplying the solid angle subtended by the Sun by the detector’s 0.25 cm^2 area (Table 4).

Table 3: Geometric inputs for spectrometer instrument response during primary observation period. These inputs assume a 280 m spherical asteroid radius, average 1 km asteroid centroid-to-spacecraft orbit, 9.84 cm mask coded area diameter, and a 20 cm focal length. During the calibration period, when REXIS observes only the sky, the entire $4.24 \text{ cm}^2\text{Sr}$ grasp is devoted to the CXB.

Parameter	Value		
	Bennu	CXB	Total REXIS
Averaged geometric detector area $A_E [\text{cm}^2]$	15.16	2.09	—
Solid angle $\Omega [\text{Sr}]$	0.254	0.185	—
Grasp $G [\text{cm}^2\text{Sr}]$	3.85	0.388	4.24

Table 4: Inputs for SXM response.

Parameter	Value
Histogram binning $\Delta E [\text{eV}/\text{bin}]$	~ 30
Single integration time	32 s
SDD area $A_E [\text{cm}^2]$	0.25
Solid angle $\Omega [\text{Sr}]$	$\pi (R_\odot/1 \text{ AU})^2 = 6.79 \times 10^{-5}$
Grasp $G [\text{cm}^2\text{Sr}]$	1.70×10^{-6}

[†]For a given differential area element on the detector surface, we calculate the solid angle subtended by Bennu and the CXB and multiply each by the differential area; we then average these values over the area of the detector.

2.2.4. Detector Quantum Efficiency

The detector quantum efficiency, $Q(E)$, gives the overall reduction in counts registered by the detector due to absorption of incoming X-rays both by material overlying the CCDs and by the CCD material itself. In the case of the CCDs, we use the known material stackup²⁷ and widely-available photoabsorption cross section data²⁸ to determine the energy-dependent attenuation and hence quantum efficiency of the detector. We also include other possible sources of detection inefficiency, including built-up molecular contamination²⁶ and the optical blocking filter (OBF), which is a thin aluminum film deposited on the CCDs in order to prevent saturation from optical light. The combined contribution of all these to $Q(E)$ is shown in Fig. 7.[‡] For the SXM, SDD efficiency curves are taken from manufacturer’s data³⁰.

2.2.5. Detector Histogram Binning

The histograms that are generated by the spectrometer data are binned in intervals of width ΔE . Photons detected by the REXIS CCDs are assigned a 9 bit energy value, so that over an energy range of 0.5 – 7.5 keV, $\Delta E = 7 \text{ keV}/2^9 \sim 15 \text{ eV}$ (Table 2). For the SXM, there are 256 energy bins, so that $\Delta E \sim 30 \text{ eV}$ (Table 4).

2.2.6. Gain Drift

Our ability to accurately define line features depends on our ability to accurately calibrate the gain of the detectors. In the case of the spectrometer, we employ on-board ⁵⁵Fe calibration sources in order to determine the line centers. The strength of the ⁵⁵Fe sources has been chosen to ensure that within a given time period, the sources’ line centers can be determined with 3σ accuracy to within one bin width. In our work, we shift the gain at 5.9 keV randomly by $\pm 15 \text{ eV}$ for each simulation we perform.

In the case of the SXM, we will use known Solar spectral features to accurately calibrate the gain over each integration period. Since the count rate for the SXM is so high, we can accurately determine line centers without counting statistics having too great an effect.

2.2.7. Detector Spectral Resolution

The detector energy resolution, which we denote by FWHM (full width half maximum), describes the width of the Gaussian distribution that a delta function-like spectral line would assume due to broadening. Natural broadening, which is typically on the order of a few eVs, is negligible in comparison to broadening from the detector itself. For the CCDs, the FWHM is a function of both photon energy and detector temperature³¹. The detector temperature drives dark current, which subsequently increases the width of the Gaussian. REXIS’s required detector operating temperature T is $-60 \text{ }^\circ\text{C}$ or below, while the predicted temperature at the time of writing is $\sim 20 \text{ }^\circ\text{C}$ colder than the requirement. Since the CCD temperature is the strongest driver of spectral resolution for a given line, and since the CCDs are passively cooled, in our results below, we calculate the performance over the range of detector temperatures between the requirement and prediction. CCD FWHM is determined using a combination of experimental data and analytical expressions, in a procedure outlined in Appendix E. Initial test results show that CCD performance is near or at Fano-limited. FWHM as a function of detector temperature for energies at the line centers of interest is shown in Fig. 7. For the SXM, the situation is somewhat simpler, since the SXM is cooled actively via a thermoelectric cooler. In this case, based on the manufacturer’s test data, we have assumed that $\text{FWHM}(5.9 \text{ keV}) = 125 \text{ eV}$.

[‡]At the time of submission of this paper, some of the quantum efficiency data shown in Fig. 7 is no longer up to date. However, the impact on our results are negligible, and future work will incorporate more accurate data. For more on the characterization of the REXIS CCDs, see Ryu, *et al.*²⁹

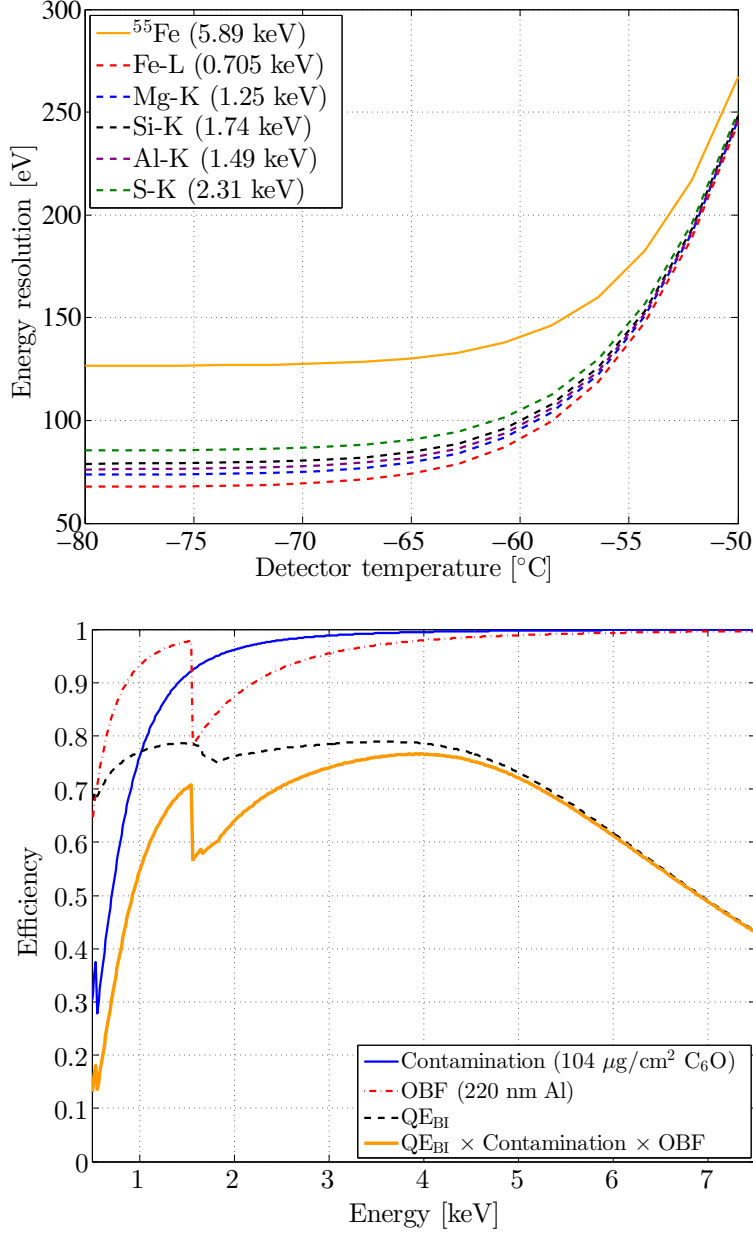


Figure 7: Drivers of spectral resolution and instrument response. In the left panel, we show the energy resolution of the CCDs as a function of detector temperature for various energies. The energies indicated are those associated with the line centers of spectral lines of interest. Initial tests have indicated that detector performance is at or near Fano-limited at the required detector operating temperature of -60°C . Curves have been calculated using the method given in Appendix E. In the right panel, we show the quantum efficiency of the CCDs as a function of energy. Several sources of efficiency degradation are indicated. Molecular contamination is indicated by the solid blue line. The effect of the optical blocking filter, whose purpose is to attenuate optical light from Bennu that could cause saturation of the detectors, is indicated by the dash-dotted red line. The dashed black line indicates the radiation attenuation due to the composition stackup of the back-illuminated CCID-41. The total effect of all these are indicated by the thick orange line. Note the quantum efficiency estimate for our back illuminated CCD includes a conservative margin.

2.2.8. Calculating the Instrument Response Function

In this section, we summarize how all the above inputs combine to generate the instrument response and a spectrum histogram. We denote the baseline intensity as $I_0(E)$ [= $I_B(E)$, $I_\odot(E)$, or $I_{\text{CXB}}(E)$] and multiply $I_0(E)$ by the relevant geometrical and time integration factors. The number of counts $C_0(E)$ accumulated by the detector over a given integration period T_{obs} is thus

$$C_0(E) = I_0(E) \cdot G \cdot T_{\text{obs}} \cdot \Delta E. \quad (1)$$

During primary observation, G for the asteroid and the CXB are those given in Table 3. During the calibration period for the CXB, however, G is that for the whole spectrometer (i.e. $4.24 \text{ cm}^2\text{Sr}$) and instead of T_{obs} , we have T_{CXB} .

$C_0(E)$ will be reduced due to the quantum efficiency of the detector, and the resulting count distribution $C_1(E)$ is given by

$$\begin{aligned} C_1(E) &= C_0(E) \cdot Q(E) \\ &= I_0(E) \cdot Q(E) \cdot G \cdot T_{\text{obs}} \cdot \Delta E. \end{aligned} \quad (2)$$

In Fig. 6, we show how Bennu's modeled spectrum compares to the CXB and internal background, plotting for each $C_1(E)/T_{\text{obs}}/\Delta E$. Consider a function $\text{Poisson}[C(E)]$ which takes as an input a number of counts for a given energy $C(E)$ and outputs a Poisson-distributed random number from a distribution whose mean is $C(E)$. Applying Poisson statistics to $C_1(E)$ then gives

$$\begin{aligned} C_2(E) &= \text{Poisson}[C_1(E)] \\ &= \text{Poisson}[I_0(E) \cdot Q(E) \cdot G \cdot T_{\text{obs}} \cdot \Delta E]. \end{aligned} \quad (3)$$

The effect of the detector state upon the spectrum is accounted for by imposing an effective broadening upon each count value in the spectrum, the broadening having the shape of a Gaussian with a given FWHM. For the CCDs, $\text{FWHM} = \text{FWHM}(E, T)$, where T is the detector temperature and E is photon energy. This broadening will not have the shape of a precise Gaussian, however, and to simulate the stochastic nature of the broadening, we generate a random distribution sampled from a Gaussian of given energy and FWHM, with the total number of counts given by $C_2(E)$. Let $\text{Gaussian}[E, C(E), \text{FWHM}(E, T)]$ denote the generic Gaussian function that takes as an input the energy E , the counts at that energy $C(E)$, and the $\text{FWHM}(E, T)$. Then the distribution of counts $C_3(E)$ is given by the convolution of Gaussian and $C_2(E)$:

$$C_3(E) = C_2(E) * \text{Gaussian}[E, C_2(E), \text{FWHM}(E, T)]. \quad (4)$$

A histogram is then generated by binning $C_3(E)$ into the required number of bins. Consider a generic binning function that takes as inputs a counts profile $C(E)$ over what may be regarded as a continuous energy range $E \in [0.5 \text{ keV}, 7.5 \text{ keV}]$ and bins it into a new profile $C'(E')$ over an energy range E' , where

$$E' = \{0.5 \text{ keV}, 0.5 \text{ keV} + \Delta E, 0.5 \text{ keV} + 2\Delta E, \dots, 7.5 \text{ keV}\}.$$

Denote this function $C'(E') = \text{Binning}[C(E), E; E']$. Then the final histogram profile $C'_3(E')$ over the binned energies is given by

$$C'_3(E') = \text{Binning}[C_3(E), E; E']. \quad (5)$$

In Fig. 8 we show a simulated histogram for a detector temperature $T = -60 \text{ }^\circ\text{C}$. For reference, the spectral features associated with our lines of interest are shown in thick colored lines. Noise subtraction (see Sec. 2.3.1 below) has been applied. In Fig. 10, we show the simulated histogram for the quiet Sun (solid magenta line), along with the idealized spectrum from which it is derived (dotted red line).

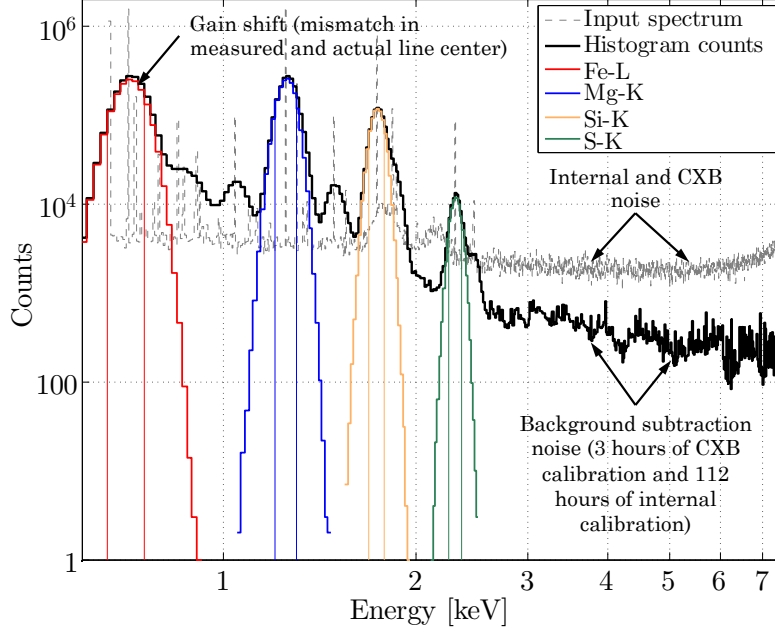


Figure 8: Example histogram of detector at temperature of -60 °C, where these results follow from our preliminary model in Fig. 6.

2.3. Data Processing

In this section, we detail our methods for processing the simulated spectrometer and SXM data (right hand and bottom side of Fig. 5). We first begin by detailing the process of noise background subtraction. Next, we discuss how we perform histogram counts for all our lines of interest. We then discuss the method for reconstructing the Solar spectrum and, finally, how we generate calibration curves to map from histogram count ratios back to elemental abundance weight ratios.

2.3.1. Spectrometer Background Subtraction

As noted, asteroid spectral features (in particular, sulfur) are sensitive to noise from the CXB and from the instrument itself. As a result, REXIS devotes periods of time for both CXB and internal noise calibration. The data gathered during the calibration period are used to subtract out sources of noise from the data product. To simulate the noise subtraction procedure, we consider the total observed histogram counts $C'_3(E')$, which includes both the internal and CXB signal. We then simulate the calibration period data. Let internal counts as a function of energy be given by $C'_{\text{int}}(E')$ and CXB counts by $C'_{\text{CXB}}(E')$, where we have assumed that Poisson statistics and binning have been performed on each, and that the counts have been accumulated over the calibration periods, T_{int} and T_{CXB} , respectively, for each. Then the procedure for background subtraction is to scale each calibration count value up so that the integration time matches that of the primary observation. Thus, the spectrum that we consider after accounting for noise subtraction is given by

$$C'_3(E') - C'_{\text{int}}(E') \frac{T_{\text{obs}}}{T_{\text{int}}} - C'_{\text{CXB}}(E') \frac{T_{\text{obs}}}{T_{\text{CXB}}}. \quad (6)$$

In Fig. 8, we see the effect of noise subtraction. The thin, dashed line shows the input spectrum with CXB and internal noise especially prominent at higher energies. After subtracting out CXB and internal background, there remains some high frequency noise (right side of Fig. 8) since Poisson statistics are included for both the simulated observation and calibration data. We note

again that, since REXIS performs its CXB calibration with a sky observation in the absence of Bennu, $C'_{\text{CXB}}(E')$ is calculated with a grasp given by that for the entire spectrometer.

2.3.2. Spectrometer Line Counting

The quantity of various elements present in Bennu’s regolith are determined by the strength of the corresponding spectral features and hence counts in the spectrometer histogram. When counting, for a given line center, we consider all the counts within the FWHM of a Gaussian centered about that line center. As discussed above, the FWHM is a function of both line center energy E and detector temperature T . Onboard calibration data, which gives us FWHM at 5.9 keV, and pre-flight test data allow us in principle to estimate the detector FWHM for each CCD frame that is processed. For the purposes of our simulations here, we assume complete knowledge of FWHM. Furthermore, as we demonstrate below (Sec. 3.1), our results are relatively insensitive to FWHM. We do not assume that we know the actual line centers with complete certainty. By employing gain drift (see Sec. 2.2.6 above), we allow for the misidentification of the line centers. In Fig. 8, we indicate the counting zones for the lines of interest by vertical lines. *All* counts within a given FWHM counting zone are considered to come from that line of interest. Therefore, there will naturally be contamination within each zone from both the continuum background, noise sources, and other lines. During our simulations, we therefore keep track of the ideal, expected count number from each line in addition to those we count directly from the histogram. The error between the two affects how well we are able to reconstruct weight ratios from these counts. More details on the counting scheme and the definition of “accuracy” are given in Appendix C.

2.3.3. Solar Spectrum Reconstruction

The method by which we use the SXM histogram to reconstruct the Solar spectrum is shown schematically in Fig. 9. First we take the quiet Sun spectrum (see Sec. 2.1.2) and convolve it with the detector response to generate a synthetic “observed” histogram (two blue boxes on the upper left of Fig. 9). Then we utilize a database of isothermal spectra which we generate beforehand and convolve those with the known detector response to generate isothermal spectrum-derived histograms (boxes on the lower left). We use the observed histogram and those generated from the database to determine a best fit. The unconvolved isothermal spectrum whose convolved form provides the best fit is used in our later analysis. In Fig. 10, we summarize the results of the fitting procedure. In Fig. 10, we see that there are good fits over the energy ranges corresponding to our elements of interest.

We have found that using a linear combination of isothermal spectra when fitting against the observed Solar spectrum can provide better fits. This result is to be expected since the realistic quiet spectrum is indeed, via integration over the DEM, a linear combination of isothermal spectra. For simplicity here, however, we focus only on single-temperature fits. The quality of the fit depends also on the characteristics of the isothermal spectrum database. These spectra are dependent on factors such as the coronal elemental abundance model employed. While we do not claim to have explored the full model space of elemental abundance models available, we have ensured that the abundance models used for both the DEM-convolved realistic spectrum and that from which the isothermal spectrum database is derived are distinct and randomly chosen.

2.3.4. Calibration Curve Generation: Mapping Count Ratios to Weight Ratios

For a given Solar state, in order to make the transition from histogram count ratios to elemental abundance ratios, we make use of so-called calibration curves¹⁴. Calibration curves map, for a given Solar state, elemental abundance ratios to ideal count ratios. To generate calibration curves, we take the unconvolved Solar spectrum and simulate asteroid spectra corresponding to a wide range of meteorite compositions. The range of elemental abundances afforded by this range allows us to consider realistic weight ratios that may be expected from Bennu. The simulated spectra allow us to determine the expected count ratios for a given weight ratio, which then allows us to map histogram counts back to elemental abundances. In Table 5, we detail the various

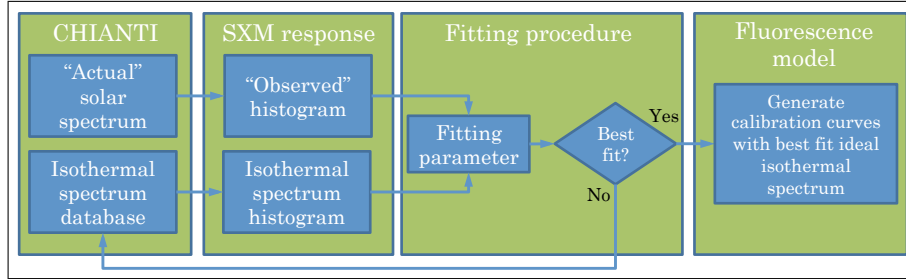


Figure 9: Solar X-ray Monitor (SXM) modeling flow. Here, we start with the “actual” Solar spectrum, which is multithermal (or equivalently, differential emission measure convolved) and which we model using the CHIANTI atomic database^{15,16} and the SolarSoftWare package¹⁷. This spectrum is convolved with the SXM instrument response function, which subsequently creates a synthetic Solar X-ray histogram data product. We rely on the fact that, in the quiet state, the Solar X-ray spectrum can be approximated as isothermal. We hence generate a database of isothermal spectra, which we likewise convolve with the SXM response function and then fit to the response-convolved quiet Sun histogram. The isothermal spectrum corresponding to the best fit isothermal histogram is then used to generate calibration curves.

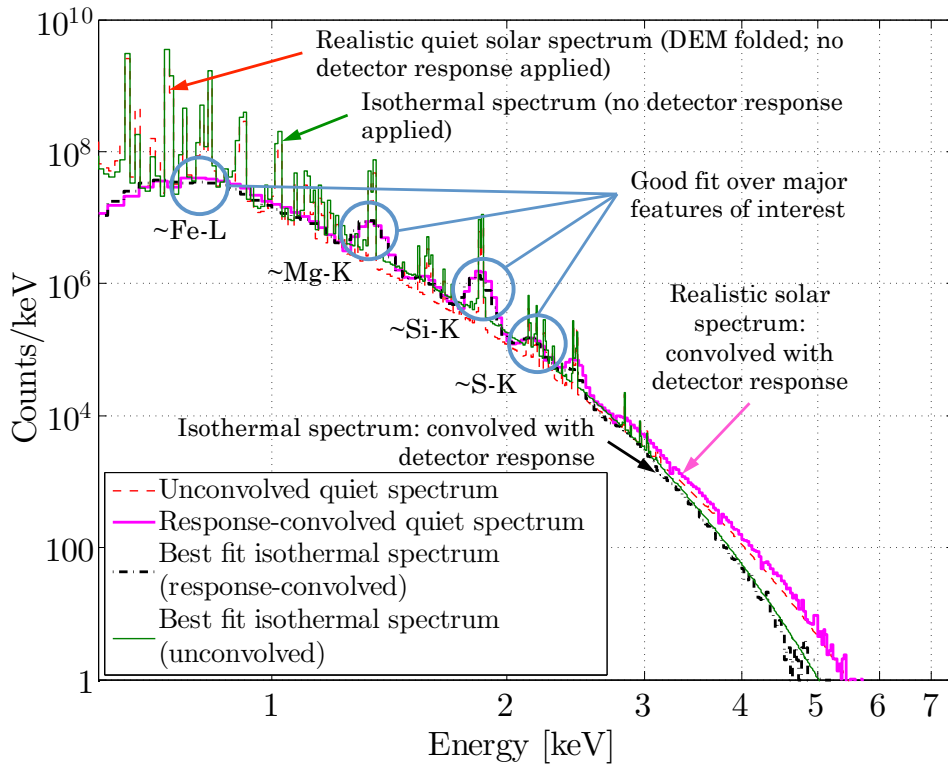
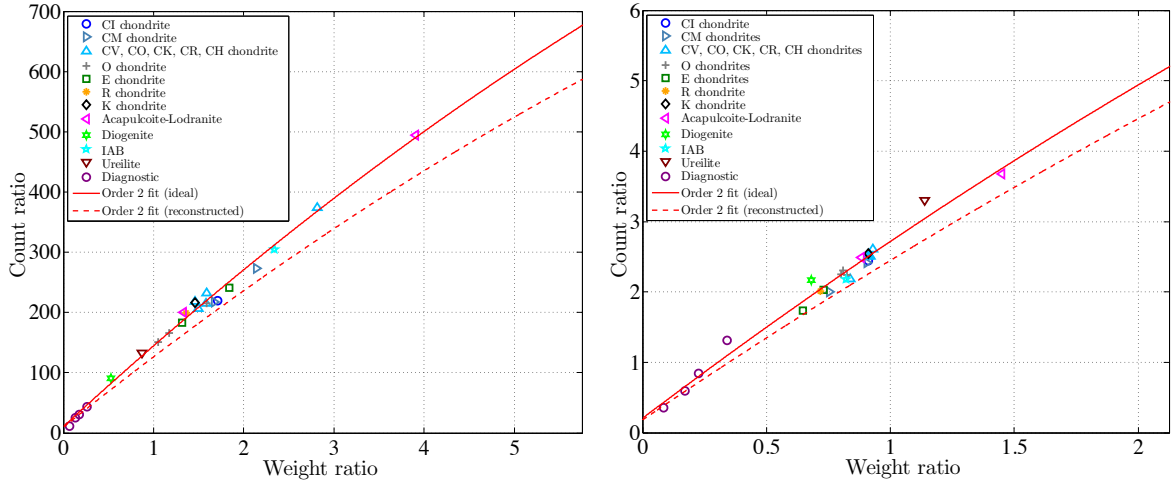


Figure 10: Fitting of quiet Solar spectra in the isothermal approximation. Example of fitting procedure for a simulated quiet Sun. First, a DEM-folded, quiet Sun Solar spectrum model is convolved with the SXM detector response function, which simulates ground data for the Solar state. Then, we search for a best fit isothermal spectrum and convolve that with the detector response function. The isothermal spectrum whose detector response has the best fit with that of the realistic spectrum is then used to generate the calibration curves (see Fig. 11). The histogram shown is over 32 s, while in this particular case, the isothermal best fit is a 3.1 MK spectrum.

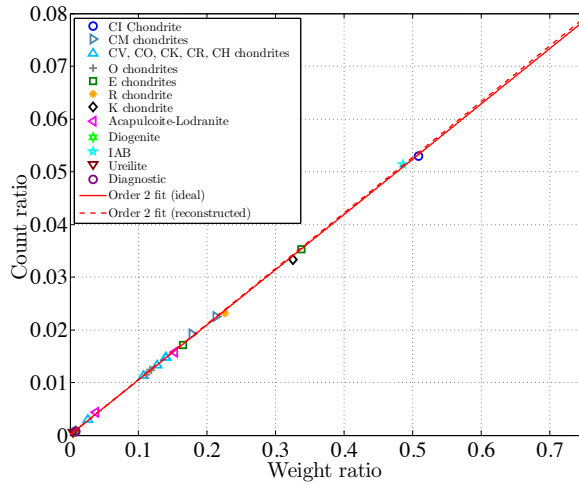
meteoritic compositions used to generate the calibrations curves for our elements of interest. In Fig. 11, we show calibration curves for our elemental ratios of interest. Various meteorite groups are indicated by the symbols. Solid lines indicate second-order fits to the realistic quiet Solar spectrum, while the dotted line indicates the fit based on the reconstructed Solar spectrum, which we discuss further below. For simplicity, we show the symbols only for the realistic quiet Sun fit and omit those for the reconstructed fit. The baseline weight ratios and expected count ratios for a CI chondrite-like regolith are indicated by the blue circles.

Table 5: Summary of inputs for calibration curves. Values are taken from Lodders and Fegley³² unless marked with “*”, in which case the data comes from Nittler, *et al.*⁹. If “—” appears, weight percent values were not available in the reference for that element, and the remainder of the percent balance was allocated to that element for the sake of the ideal asteroid spectrum simulation. Since O is not one of our elements of interest, the development of the calibration curves is not incumbent upon accurate knowledge of O.

Class	Weight percent by element					
	O	Mg	Al	Si	S	Fe
CI	46.4	9.70	0.865	10.64	5.41	18.2
CM	43.2	11.5	0.130	12.70	2.70	21.3
CM*	38.92	8.99	1.334	11.916	2.122	25.466
CV	37.0	14.3	1.680	15.70	2.20	23.5
CO	37.0	14.5	1.400	15.80	2.20	25.0
CK	—	14.7	1.470	15.80	1.70	23.0
CR	—	13.7	1.150	15.00	1.90	23.8
CH	—	11.3	1.050	13.50	0.35	38.0
H	35.70	14.1	1.06	17.1	2.0	27.2
L	37.70	14.9	1.16	18.6	2.2	21.75
LL	40.00	15.3	1.18	18.9	2.1	19.8
EH	28.00	10.73	0.82	16.6	5.6	30.5
EL	31.00	13.75	1.00	18.8	3.1	24.8
R	—	12.9	1.06	18.0	4.07	24.4
K	—	15.4	1.30	16.9	5.5	24.7
Acap.*	—	15.6	1.20	17.7	2.7	23.5
Lod.*	25.858	16.299	0.0952	11.248	0.4257	43.92
Dio.*	20.42	16.528	1.00	24.28	0.204	12.729
IAB*	26.62	11.92	1.31	14.48	7.04	33.9



(a) Fe/Si weight ratio to count ratio calibration curve. (b) Mg/Si weight ratio to count ratio calibration curve.



(c) S/Si weight ratio to count ratio calibration curve.

Figure 11: Weight ratio to count ratio calibration curves for the elemental abundance ratios of interest. Calibration curves are a function of weight ratio and Solar spectrum. Curves indicate second order fits to simulated spectra of asteroids with the same composition as the major meteorite types indicated (see Table 5). Several artificial, “diagnostic” compositions have also been included to improve the fidelity of the fit. The solid curve indicates spectra generated using the DEM-folded quiet Solar spectrum. The dotted curve indicates spectra generated using the isothermal best fit (see Fig. 10). The baseline weight ratios and expected count ratios for a CI chondritic-like regolith are indicated by the blue circles.

3. Results

In this section, we detail our results based on the simulations and analysis presented in the previous sections. We first show how, assuming perfect knowledge of the Solar state, the count ratios we measure map back to elemental abundance weight ratio errors with respect to CI chondrite-like baseline composition. Next, based on these count ratio errors, we present the required observation times to achieve statistical significance on our measurements. Finally, we present a qualitative discussion of how the error generated during Solar spectrum reconstruction develops a permissible error space in which we interpret our results.

3.1. Weight Ratio Accuracy

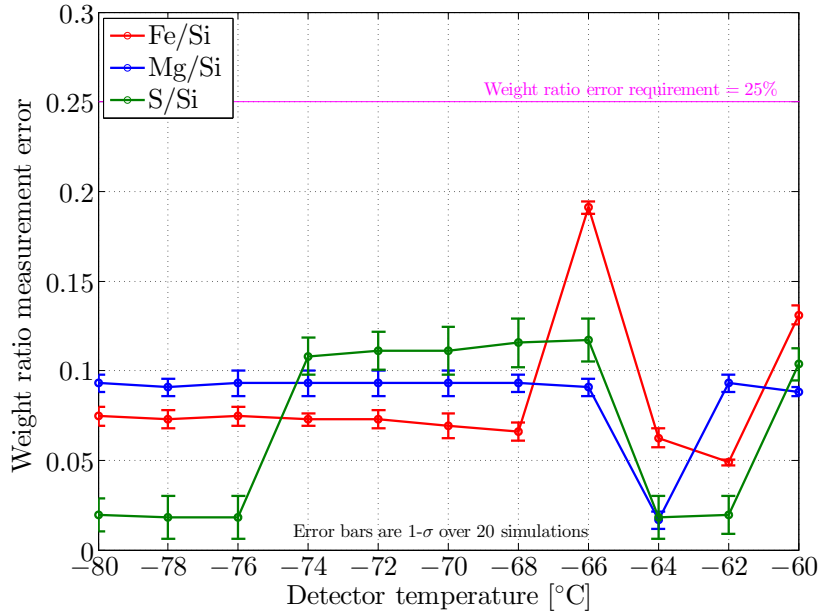
Using the calibration curves given in Fig. 11, we can map the errors incurred by our histogram counting procedure into subsequent errors in weight ratio. In general, since the relationship between counts and regolith weight is roughly linear, the correspondence between count ratio error and weight ratio error is also roughly linear. In Table 6, we list the weight ratio errors for our required detector temperature ($T = -60$ °C) and our current best prediction for the detector temperature ($T \sim -80$ °C). In all cases, the predicted error is less than the requirement. The weight ratio errors over the range of temperatures between $T = -60$ °C and -80 °C are shown on the left panel of Fig. 12. The error bars in the figure represent the error spread over 20 simulations at each detector temperature, with each simulation incorporating the effect of factors such as Poisson statistics, gain drift, and noise subtraction. We note that, over most of the temperatures, there is not necessarily a degradation of performance with increasing detector temperature, as we might naively expect due to the decrease in spectral resolution. The relative insensitivity of our spectral performance on detector temperature (or equivalently FWHM) is primarily due to the fact that taking count ratios effectively cancels some of the effect of this systematic error present in each of the individual lines. In Fig. 4, we indicate with magenta ellipses the accuracy error due to these systematic effects at $T = -60$ °C.

Table 6: Summary of REX-3 systematic accuracy error performance. We show the accuracy error for each elemental abundance ratio of interest at two different detector temperatures. The detector temperature of -60 °C represents the required detector operating temperature, while -80 °C represents the current best prediction for the detector temperature at the time of writing.

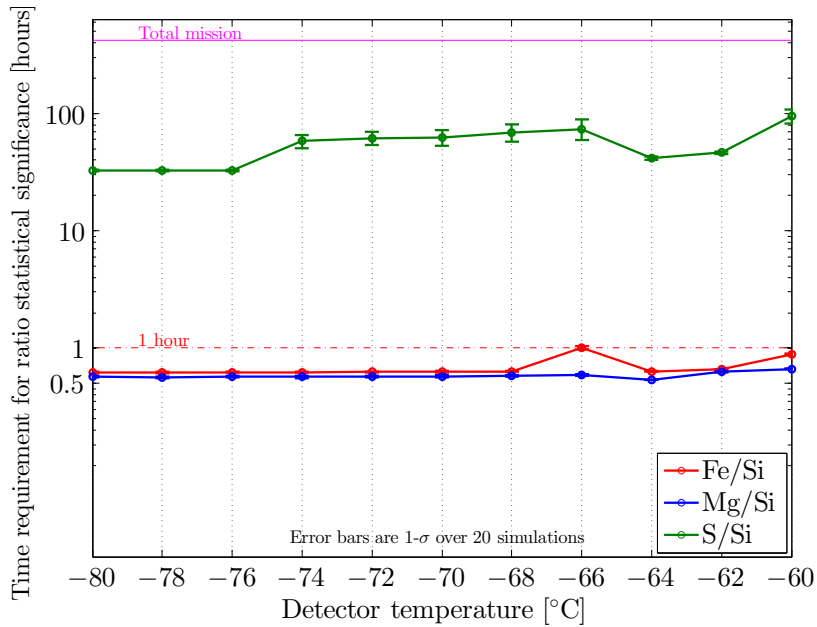
Det. Temp. T		Ratio	Predicted accuracy error [%]	Requirement [%]	Margin (Requirement/Prediction)
		-60 °C	Fe/Si	13.7	$\leq 25\%$
Mg/Si	9.1		$\leq 25\%$	2.7	
S /Si	10.3		$\leq 25\%$	2.4	
-80 °C	Fe/Si	7.9	$\leq 25\%$	3.2	
	Mg/Si	9.7	$\leq 25\%$	2.6	
	S /Si	3.0	$\leq 25\%$	8.3	

3.2. Observation Time

The results in the above section represent systematic error. That is, they represent errors intrinsic to the behavior of the instrumentation itself. We must also consider statistical error to account for the stochastic nature of photon emission and place a statistical significance on our expected results. In order to account for statistical error, we consider the quadratic difference between our expected *count* ratio error and allowed count ratio error. Then, assuming Poisson statistics, based on the count rates within each energy range of interest from both the fluorescent lines and noise sources, we determine the required observation time to achieve an $N\sigma$ statistical significance level. Here, we choose $N = 3.5$, corresponding to $> 99\%$ confidence. A detailed calculation of



(a) Weight ratio error as a function of detector temperature.



(b) Observation time requirement to achieve statistical significance.

Figure 12: Spectral simulation results assuming perfect knowledge of the Solar state. In the left panel, we show the weight ratio error for our line ratios of interest as a function of detector temperature. The 25% requirement is indicated by the magenta line. For all temperatures, we are able to meet our requirement with margin. In the right panel, we show the observation time required to achieve statistical significance on our spectral measurements. The requirement that we achieve significance within the allotted mission time is shown by the magenta line. The observation time is derived from the count rates from the lines of interest, CXB, and internal noise, and from the difference between predicted accuracy error and required accuracy error. S/Si, which is most susceptible to noise from the internal background and CXB, requires the greatest observation time. Error bars are 1σ over 20 simulations.

the above, as well as expected count rates, is given in Appendix D and Table 9, respectively. Our required observation times for the two detector temperatures discussed above are given in Table 7, while those for the range of temperatures in between are given in the right panel of Fig. 12. Again, in all cases, we are able to achieve our required performance with margin. As noted above, the S/Si ratio, which is most subject to the effect of CXB and internal noise, requires the greatest amount of observation time to achieve statistical significance. The magenta error ellipses shown in Fig. 4 thus have a 3.5σ statistical confidence associated them.

Table 7: Summary of REX-6 observation time requirement expected performance for detector temperature of $-60\text{ }^\circ\text{C}$ and $-80\text{ }^\circ\text{C}$. The observation time is based on obtaining sufficient photon statistics to achieve 3.5σ confidence in the accuracy results.

		Ratio	Observation time for 3.5σ confidence [hours]	Requirement [hours]	Margin (Requirement/Prediction)
Det. Temp. T	$-60\text{ }^\circ\text{C}$	Fe/Si	0.9	≤ 420	467
		Mg/Si	0.7	≤ 420	600
		S/Si	108	≤ 420	3.9
	$-80\text{ }^\circ\text{C}$	Fe/Si	0.6	≤ 420	700
		Mg/Si	0.6	≤ 420	700
		S/Si	33	≤ 420	12.7

3.3. Calibration Curves and Mapping Errors

In the results above, we have assumed perfect knowledge of the Solar state in mapping count ratio errors to weight ratio errors. Hence, we have used the solid red calibration curves shown in Fig. 11. In reality, we will have to use the reconstructed Solar spectrum-derived calibration curves (dotted red lines in Fig. 11) in order to perform the mapping. From the calibration curves shown in Fig. 11, it is clear that the difference between the curves based on the actual and reconstructed Solar spectra are within the error of the fit itself over the weight ratio ranges of interest, so that we cannot claim a truly meaningful difference between the quality of each fit. While we have not accounted for this effect in the results presented above, we demonstrate graphically in Fig. 13 the error space that develops from reconstructing the Solar spectrum. Fig. 13 shows how, in the most extreme case (Fe/Si) the calibration curves diverge for the different input Solar spectra. The lines marked “baseline” map to a CI chondrite-type composition under the actual Solar spectrum. The 25% identification requirement then places a range of permissible errors about this baseline (the shaded grey area). So long as the combined misidentification of the Solar spectrum and the count ratio error does not exceed the bounds set by the shaded region, REXIS can still achieve its objectives. In our case, for the $T = -60\text{ }^\circ\text{C}$ case, the Fe/Si error is the most marginal (13.7% error), although it still falls within the required performance region. Since Fe/Si is not subject to the the same statistical fluctuation as e.g. S/Si, statistical significance on Fe/Si can still easily be achieved within the allotted observation time.

4. Discussion and Conclusions

In the previous sections, we have presented the methodology and results of spectral performance modeling of REXIS. We have shown, by simulating Solar and asteroid X-ray spectra, the subsequent data product, and the data processing, how well REXIS can be expected to identify Bennu as a CI chondrite analog. We have shown that our two primary requirements—that REXIS is capable of identifying a baseline CI chondrite meteorite analog for Bennu to within 25% and that it can accomplish this within the allotted mission observation time—are attainable with margin.

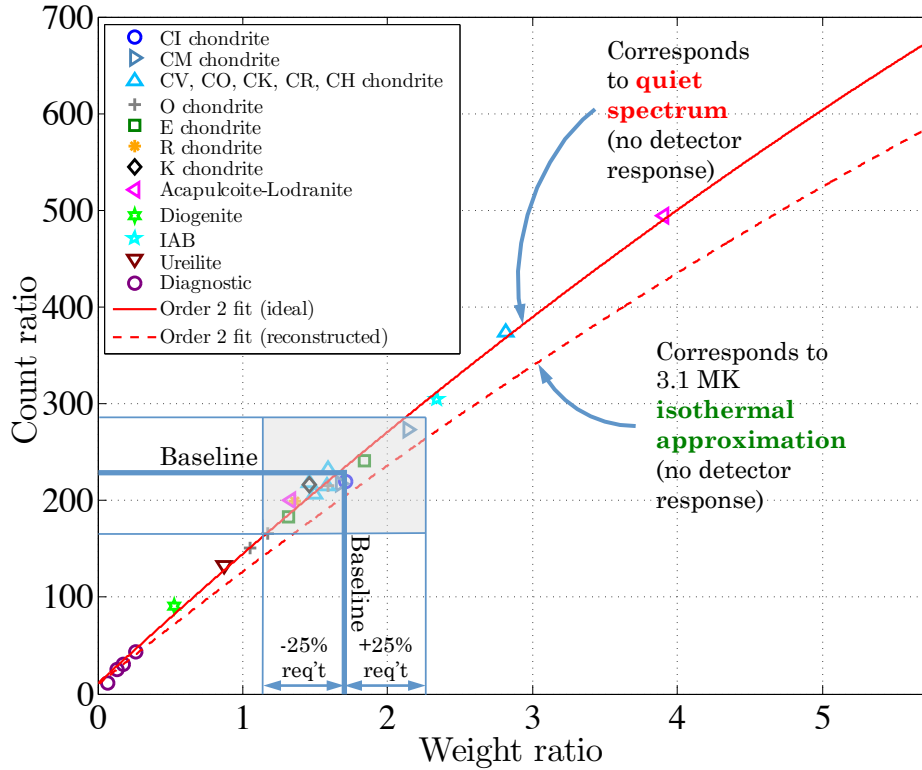


Figure 13: Calibration curve error space. The solid red line is the calibration curve generated by the quiet Sun (red line in Fig. 10). This is the calibration curve that would be generated if we had perfect knowledge of the Solar state. The dashed red line is the calibration curve generated by the best single temperature fit based on simulated SXM data (green line in Fig. 10).

4.1. Future Work

This work represents the first step in understanding REXIS’s science performance in Spectral Mode, and there are numerous opportunities to extend and refine this work. We summarize some of these below.

4.1.1. Other Baseline Regolith Compositions for Bennu

Throughout this work, we have assumed a baseline CI chondrite-like regolith composition for Bennu. In reality, ground measurements have suggested a possible CM chondrite-like composition. While we should not expect any substantial difference in expected performance if we assumed a CM-type composition, it is worthwhile to consider the possibility that the baseline composition of the regolith is something radically different (for instance, achondritic).

4.1.2. Higher Order Observational Effects

We have assumed here that the orbit is perfectly circular and that Bennu is a perfect sphere, e.g. we do not take into account surface roughness. However, it is possible to use the Bennu shape model³³ and OSIRIS-REx orbit for REXIS science operations in order to model the effect of both shape and orbit to a higher level of fidelity.

4.1.3. Active Sun Modeling and Reconstruction

We have assumed throughout this work that the Sun is in a quiet state, which it will be for the majority of REXIS's science operations. However, the Sun will occasionally flare, creating a higher flux and harder (i.e. greater intensity at higher energies) spectrum. This in turn will substantially affect Bennu's spectrum. Performing a similar analysis to the above, but assuming a flare Sun, should be carried out. The flare Sun, however, cannot be approximated as isothermal, although a two-temperature model may suffice [see Appendix B and also Lim and Nittler (2009)¹⁴].

4.1.4. Improved SXM Modeling

In this work, we have assumed a relatively simple geometry and instrument response function for the SXM. Much as we have done for the spectrometer, it is possible to compute higher fidelity values for the SXM grasp and, with continued testing, better characterize the SXM response function in general.

4.1.5. Radiation Damage

Preliminary work has suggested that under OSIRIS-REx's expected radiation environment, degradation in CCD spectral resolution due to non-ionizing radiation damage still permits REXIS to meet its science objectives. This is in part due to the presence of the radiation cover^{34,35,7} and the fact that REXIS is primarily concerned with the measurement of count ratios, which reduces the effect of spectral degradation on weight ratio reconstruction error. (Sec. 3.1). However, continued characterization of the REXIS CCDs should allow for a more definite characterization of REXIS's radiation environment and the effect of radiation damage on spectral performance (especially as a function of time), which we have not accounted for here.

4.1.6. Internal Background

The internal background spectrum we have used here is scaled from Chandra data. In the future, a more accurate model making use of the actual REXIS geometry should be employed to determine the fluorescent signature of the REXIS structure in response to X-rays from Bennu and the CXB. In this case, a simulation framework such as GEANT4³⁶ can be used to determine the intensity of X-ray emission from REXIS itself incident upon the CCDs.

4.1.7. Further Exploration of Error Space

While our discussion of the error space in Sec. 3.3 was somewhat qualitative, it is worthwhile to be more quantitative about our approach. Furthermore, we may continue to characterize how each of the model inputs discussed in Sec. 2 (such as molecular contamination, the OBF, and the spectral resolution) independently affect spectral performance.

Acknowledgments

The authors would like to thank Dr. Steve Kissel of the MIT Kavli Institute for CCD test data, Beverly LaMarr of the MIT Kavli Institute for discussions regarding radiation damage to CCDs, and Dr. Lucy Lim of NASA GSFC and Dr. Ben Clark of the Space Science Institute for many helpful discussions and suggestions concerning asteroid spectroscopy. This work was conducted under the support of the OSIRIS-REx program through research funds from Goddard Space Flight Center.

A. Modeling Benu

A.1. Fluorescence

We model Benu as a sphere of 280 m radius, with OSIRIS-REx viewing Benu in a terminator orbit at 1 km from the asteroid barycenter. Denote a point on Benu by P , the center of REXIS's detector plane by R , and the center of mass of the Sun by S . Let the angle between surface normal at P and \overline{SP} be given by ψ_{in} , and that between the surface normal at P and \overline{PR} by ψ_{out} . Then the intensity for the k^{th} fluorescence line as measured by REXIS is given by¹¹

$$I_k(E_k) = \frac{\Omega_{\odot}}{\Omega_B} \int_{\text{Benu}} \frac{d\Omega_B Q_k(E_k)}{4\pi \Delta E \sin \psi_{\text{in}}} \int_{E_k}^{\infty} \frac{I_{\odot}(E) dE}{\sum_j W_j [\mu_j(E) \csc \psi_{\text{in}} + \mu_j(E_k) \csc \psi_{\text{out}}]} \quad (7)$$

where $Q_k(E_k)$ is a factor that encompasses the probability and quantum yield associated with emission of the k^{th} line. Ω_{\odot} is the solid angle subtended by the Sun with respect to Benu, ΔE is an arbitrarily-chosen energy bin, and Ω_B is the solid angle subtended by Benu with respect to REXIS. If we assume all incident Solar X-rays are parallel to one another (valid since the Sun can effectively be considered a point source with respect to Benu), then ψ_{in} , ψ_{out} , and $d\Omega_B$ can be related to one another by straightforward geometry, and an integration over the entire surface area of Benu amounts to an integration over all the ψ_{out} within the REXIS field of view.

If W_k is the weight fraction of the element associated with the k^{th} line, r_k is the jump ratio, ω_k is the fluorescence yield, and f_k is the fraction of the series to which k belongs that is devoted to k , we have

$$Q_k(E_k) = W_k \frac{r_k - 1}{r_k} \omega_k f_k. \quad (8)$$

Since fluorescent intensity is monochromatic, the total contribution to the spectrum from fluorescence is the sum of all the I_k . An example of the calculation of the line/probability factor for the Fe-K series is given in Table 8.

Table 8: Series information for Fe-K and calculation of associated line probability/yield factor, $Q_k(E_k)$.

Edge/Series	r_k	ω_k	Line	E_k [eV]	f_k	Q_k/W_k
Fe-K	0.351	7.893	K α_3	6,267.40	2.76096×10^{-4}	7.649×10^{-4}
			K α_2	6,392.10	2.94023×10^{-1}	8.145×10^{-1}
			K α_1	6,405.20	5.80277×10^{-1}	1.608
			K β_3	7,059.30	4.25566×10^{-2}	1.179×10^{-1}
			K β_1	7,059.30	8.21556×10^{-2}	2.276×10^{-1}
			K β_5	7,110.00	7.12115×10^{-4}	1.973×10^{-3}

A.2. Coherent scattering

The continuous spectrum due to coherent scattering is given by

$$I_{\text{scattering}}(E) = \frac{1}{\Omega_B} \int_{\Omega} \frac{d\sigma}{d\Omega} I_{\odot}(E) N_A d\Omega_B, \quad (9)$$

where N_A is Avogadro's number and the integration effected over the solid angle Ω . The differential scattering cross section $d\sigma/d\Omega$ is given by

$$\frac{d\sigma}{d\Omega} = \frac{r_e^2}{4\pi} (1 - \cos^2 \theta) |F(E, \theta)|^2, \quad (10)$$

where r_e is the classical electron radius, given by 2.82×10^{-15} m, and where $|F(E, \theta)|^2$ the modulus squared of the (complex) atomic form factor $F(E, \theta)$ for the element in question, dependent upon both the energy of the incident radiation and the scattering angle $\theta \equiv |\psi_{\text{in}} + \psi_{\text{out}}|$. Incoherent scattering, being at least an order of magnitude smaller than coherent scattering for all energies and elements of interest, is not considered. The total intensity of radiation emitted by the asteroid (in units of photons/Sr/s/eV/cm²) is given by the sum of fluorescent and scattered radiation:

$$I(E) = \sum_k I_k(E_k) + I_{\text{scattering}}(E). \quad (11)$$

B. Modeling the Solar Spectrum

Here we briefly discuss how the Solar corona is modeled in order to determine its X-ray spectrum. Denote the power per unit volume emitted by a plasma undergoing an atomic transition from quantum states $j \rightarrow i$ by P_{ij} , and the wavelength (or equivalently, the energy) associated with this transition by λ_{ij} . Then the intensity $I_{\odot}(\lambda_{ij})$ of the radiation at the surface of the body of interest (say Benu) for this transition is given by

$$I_{\odot}(\lambda_{ij}) = \frac{1}{4\pi R^2} \int_V P_{ij} dV, \quad (12)$$

where R is the distance from the Sun to Benu and V is the plasma volume. P_{ij} can be written²¹

$$P_{ij} = 0.8A_X G(T, \lambda_{ij}) \frac{hc}{\lambda_{ij}} N_e^2, \quad (13)$$

where N_e is the local electron density, A_X is the abundance of the X th element with respect to hydrogen, and G is the so-called contribution function (not to be confused with the grasp), which is a function of both the plasma temperature T (not to be confused with the detector temperature) and the wavelength λ_{ij} associated with the transition.

P_{ij} is dependent upon both temperature and electron density, and it is possible to decompose it into density and temperature dependent parts. We define the ‘‘differential emission measure’’, or DEM, as follows

$$\int_V N_e^2 dV = \int_T \text{DEM}(T) dT, \quad (14)$$

so that

$$P_{ij} = 0.8A_X G(T, \lambda_{ij}) \frac{hc}{\lambda_{ij}} \text{DEM}(T) \frac{dT}{dV}. \quad (15)$$

On the left hand side of Eq. (14), the integration is effected over the plasma volume; on the right hand side, over the possible coronal temperatures. Defining

$$\phi(T, \lambda) \equiv \sum_X \sum_{ij} 0.8A_X G(T, \lambda_{ij}) \frac{hc}{\lambda_{ij}} \quad (16)$$

(the first sum extending over all species and the second sum extending over all transition pairs), we have, using Eq. (14),

$$I_{\odot}(\lambda) = \int_T \phi(T, \lambda) \text{DEM}(T) dT. \quad (17)$$

Instead of integrating over all possible coronal temperatures, in certain cases, it is possible to consider only those coronal temperatures at which the emission measure is greatest. For quiet

Solar regions, it has been found that the emission measure peaks at one value, while the DEM for active regions tends to peak at two values. Thus we may write

$$I_{\odot}(\lambda) = \phi(T_1, \lambda)EM(T_1) \quad (\text{quiet Sun}) \quad (18)$$

$$I_{\odot}(\lambda) = \phi(T_1, \lambda)EM(T_1) + \phi(T_2, \lambda)EM(T_2) \quad (\text{active Sun}) \quad (19)$$

where $EM(T)$ is a single temperature emission measure, which for all practical purposes here amounts to a simple numerical prefactor.

C. Definition of Accuracy

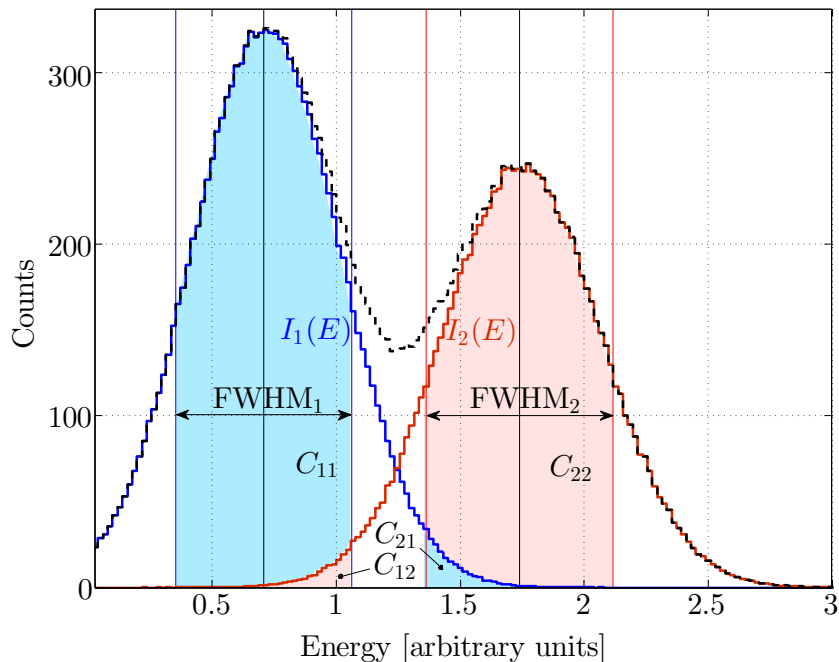


Figure 14: Example of line contamination in the simplified case of only two lines, $I_1(E)$ (blue) and $I_2(E)$ (red); their sum is in black. The counts $C_{11} + C_{12}$ account for all the counts under the sum in the FWHM zone of line 1 and the counts $C_{22} + C_{21}$ are all the counts in the FWHM zone of line 2. C_{11} are the counts that are due to line 1 in the line 1 FWHM zone, and C_{22} are the counts due to line 2 in the line 2 FWHM zone, while C_{12} is the contamination from line 2 into the FWHM zone of line 1, and C_{21} the contamination of line 1 into the FWHM zone of line 2.

REXIS's spectral performance requirement states that the reconstructed weight ratios of the asteroid regolith be within a certain percent of that of the baseline composition. REXIS itself can only measure count ratios, and we use the calibration curves to make the correspondence between count ratios and weight ratios. For convenience, we denote this function CC : count ratio \rightarrow weight ratio, with the inverse mapping CC^{-1} : weight ratio \rightarrow count ratio.

Fig. 14 demonstrates REXIS's counting procedure in forming count ratios. For simplicity, the figure shows only two spectral features I_1 and I_2 , shown in blue and red, respectively. First, we define counting zones centered about each line center. The width of these zones are given by the full-width half-maximum FWHM of the Gaussian centered at each energy. All the counts within each zone are considered to be from the respective line, although in reality, there will be some contamination from other spectral features. Thus in our simplified case, the total number of counts in $FWHM_1$ will include contributions from I_1 , denoted C_{11} , and those from I_2 , denoted C_{12} .

Likewise, the total number of counts in FWHM_2 will include contributions from I_2 (given by C_{22}) and I_1 (given by C_{21}). The total count ratio of the first feature to the second $\rho_{1/2}$ is then given by

$$\rho_{1/2} = \frac{C_{11} + C_{12}}{C_{22} + C_{21}}. \quad (20)$$

In the more general case applicable to REXIS, we have the total number of binned detector counts given by $C'_3(E')$, so that for the $\rho_{k/\text{Si}}$ line ratio,

$$\rho_{k/\text{Si}} = \frac{\sum_{E_k - \text{FWHM}_k/2}^{E_k + \text{FWHM}_k/2} C'_3(E')}{\sum_{E_{\text{Si}} - \text{FWHM}_{\text{Si}}/2}^{E_{\text{Si}} + \text{FWHM}_{\text{Si}}/2} C'_3(E')}. \quad (21)$$

We map $\rho_{k/\text{Si}}$ to the equivalent weight ratio $\varpi_{k/\text{Si}}$ by using the calibration curve: $\varpi_{k/\text{Si}} = \text{CC}(\rho_{k/\text{Si}})$. The accuracy error is then calculated by comparing the measured weight ratio $\varpi_{k/\text{Si}}$ with the regolith input weight ratio $\varpi_{k/\text{Si},0}$ corresponding to a CI chondrite-like composition. If we denote the weight ratio error requirement by η , then we may write the requirement as

$$\left| 1 - \frac{\varpi_{k/\text{Si}}}{\varpi_{k/\text{Si},0}} \right| \leq \eta, \quad (22)$$

where $\eta = 0.25$.

In some cases (e.g., Appendix D), we may wish to consider only the errors in count ratios. In this case, we consider the expected count ratio from the lines of interest, ignoring contamination and other effects. If we denote this ratio by $\rho_{k/\text{Si},0}$, we have

$$\rho_{k/\text{Si},0} = \frac{C_1(E_k)}{C_1(E_{\text{Si}})}, \quad (23)$$

where care has been taken to ensure that the effect of quantum efficiency has been accounted for. Indeed, when the calibration curves are generated, $\rho_{k/\text{Si},0}$ is calculated for a whole range of baseline compositions, and a second order fit performed on the various $(\varpi_{k/\text{Si},0}, \rho_{k/\text{Si},0})$ pairs (Fig. 11). The REXIS performance requirement in terms of count ratio is denoted by η_C , and is then given by

$$\left| 1 - \frac{\rho_{k/\text{Si}}}{\rho_{k/\text{Si},0}} \right| \leq \eta_C. \quad (24)$$

η_C can be related to η in a relatively straightforward way that is most clearly demonstrated graphically by means of the shaded region shown in Fig. 13; it is given mathematically by

$$\left| 1 - \frac{\text{CC}^{-1}[(1 - \eta) \times \varpi_{k/\text{Si},0}]}{\text{CC}^{-1}(\varpi_{k/\text{Si},0})} \right| = \eta_C. \quad (25)$$

D. Statistical Error

Suppose for a given detector temperature that the total error in counts due to systematic error is Δ , that the requirement is given by η_C , and that statistical error is given by σ . We suppose that the errors can be summed quadratically:

$$\eta_C = \sqrt{\Delta^2 + \sigma^2}, \quad (26)$$

so that

$$\sigma = \sqrt{\eta_C^2 - \Delta^2}. \quad (27)$$

For the k^{th} line and an N confidence level,

$$\frac{\sigma^2}{N^2} = \frac{\dot{N}_k/T_{\text{tot}} + \dot{N}_{\text{CXB},k}/T_{\text{CXB}} + \dot{N}_{\text{int},k}/T_{\text{int}}}{\left(\dot{N}_k - \dot{N}_{\text{CXB},k} - \dot{N}_{\text{int},k}\right)^2} + \frac{\dot{N}_{\text{Si}}/T_{\text{tot}} + \dot{N}_{\text{CXB},\text{Si}}/T_{\text{CXB}} + \dot{N}_{\text{int},\text{Si}}/T_{\text{int}}}{\left(\dot{N}_{\text{Si}} - \dot{N}_{\text{CXB},\text{Si}} - \dot{N}_{\text{int},\text{Si}}\right)^2}. \quad (28)$$

T_{CXB} and T_{int} are the CXB and internal calibration times (see Sec. 2.3.1). \dot{N}_k , $\dot{N}_{\text{CXB},k}$, and $\dot{N}_{\text{int},k}$ refer respectively to the total count rates, CXB count rates, and internal background count rates within the k^{th} FWHM counting zone. More precisely, \dot{N}_k , $\dot{N}_{\text{CXB},k}$, and $\dot{N}_{\text{int},k}$ are given by C'_3/T_{obs} , $C'_{\text{CXB}}/T_{\text{obs}}$, and $C'_{\text{int}}/T_{\text{obs}}$ summed over each FWHM zone. Rearranging Eq. 28, we get

$$\begin{aligned} \frac{\sigma^2}{N^2} &= \left[\frac{\dot{N}_k}{\left(\dot{N}_k - \dot{N}_{\text{CXB},k} - \dot{N}_{\text{int},k}\right)^2} + \frac{\dot{N}_{\text{Si}}}{\left(\dot{N}_{\text{Si}} - \dot{N}_{\text{CXB},\text{Si}} - \dot{N}_{\text{int},\text{Si}}\right)^2} \right] \frac{1}{T_{\text{tot}}} + \\ &\underbrace{\frac{\dot{N}_{\text{CXB},k}/T_{\text{CXB}} + \dot{N}_{\text{int},k}/T_{\text{int}}}{\left(\dot{N}_k - \dot{N}_{\text{CXB},k} - \dot{N}_{\text{int},k}\right)^2} + \frac{\dot{N}_{\text{CXB},\text{Si}}/T_{\text{CXB}} + \dot{N}_{\text{int},\text{Si}}/T_{\text{int}}}{\left(\dot{N}_{\text{Si}} - \dot{N}_{\text{CXB},\text{Si}} - \dot{N}_{\text{int},\text{Si}}\right)^2}}_{\equiv R}. \end{aligned} \quad (29)$$

With L and R defined as above, the total observation time T_{obs} required for $N\sigma$ confidence is given by

$$T_{\text{obs}} = \frac{L}{R - \sigma^2/N^2}. \quad (30)$$

A summary of the expected count rates within each FWHM zone are given in Table 9.

Table 9: Summary of expected count rate with detector temperature $T = -60$ °C. E_- and E_+ are the lower and upper limits to the FWHM zone for each line, respectively. \dot{N}_k is the total number of counts in each FWHM zone (i.e., from Bennu and background), while $\dot{N}_{\text{CXB},k}$ and $\dot{N}_{\text{int},k}$ are CXB and internal count rates, respectively, in each zone.

Line	E_- [keV]	E_+ [keV]	\dot{N}_k	$\dot{N}_{\text{int},k}$	$\dot{N}_{\text{CXB},k}$
Fe-L	0.658	0.751	4.73	0.038	3.73
Mg-K	1.1830	1.3230	2.64	0.0291	1.69
Si-K	1.6620	1.8139	1.46	0.0745	0.948
S-K	2.2250	2.3910	0.967	0.0296	0.888

E. Calculating the Energy Resolution of the Detector

To determine the energy and detector temperature dependence of the detector resolution FWHM, we require two pieces of experimental data: FWHM as a function of energy E at a fixed temperature T_0 , and FWHM as a function of temperature T at a fixed energy E_0 . The two pieces of information can be combined then to determine the general dependence of FWHM on E and T [§]:

$$\text{FWHM}(E, T) = \sqrt{\text{FWHM}^2(E, T_0) + \text{FWHM}^2(E_0, T) - \text{FWHM}^2(E_0, T_0)} \quad (31)$$

In the case of REXIS, energy resolution for the CCID-41 has been experimentally determined as a function of energy at $T_0 = -90$ °C[¶], and as a function of temperature at $E_0 = 5.89$ keV^{||}. These two pieces of information together allow us to use Eq. 31 to generate Fig. 7.

[§]Personal communication, M. Bautz.

[¶]Personal communication, M. Bautz.

^{||}Personal communication, S. Kissel.

References

- [1] Lauretta, D. S. and OSIRIS-Rex Team, “An Overview of the OSIRIS-REx Asteroid Sample Return Mission,” in [*Lunar and Planetary Science Conference*], *Lunar and Planetary Science Conference* **43**, 2491 (Mar. 2012).
- [2] Clark, B. E., Binzel, R. P., Howell, E. S., Cloutis, E. A., Ockert-Bell, M., Christensen, P., Barucci, M. A., DeMeo, F., Lauretta, D. S., Connolly Jr, H., et al., “Asteroid (101955) 1999 RQ36: Spectroscopy from 0.4 to 2.4 μm and meteorite analogs,” *Icarus* **216**(2), 462–475 (2011).
- [3] Campins, H., Morbidelli, A., Tsiganis, K., De Leon, J., Licandro, J., and Lauretta, D., “The origin of Asteroid 101955 (1999 RQ36),” *The Astrophysical Journal Letters* **721**(1), L53 (2010).
- [4] Milani, A., Chesley, S. R., Sansaturio, M. E., Bernardi, F., Valsecchi, G. B., and Arratia, O., “Long term impact risk for (101955) 1999 RQ36,” *Icarus* **203**(2), 460–471 (2009).
- [5] Allen, B., Grindlay, J., Hong, J., Binzel, R. P., Masterson, R., Inamdar, N. K., Chodas, M., Smith, M. W., Bautz, M. W., Kissel, S. E., et al., “The REgolith X-Ray Imaging Spectrometer (REXIS) for OSIRIS-REx: identifying regional elemental enrichment on asteroids,” in [*SPIE Optical Engineering+ Applications*], 88400M–88400M, International Society for Optics and Photonics (2013).
- [6] Jones, M. P., Smith, M. J., and Masterson, R. A., “Engineering Design of the REgolith X-ray Imaging Spectrometer (REXIS) Instrument: An OSIRIS-REx Student Collaboration,” in [*SPIE Optical Engineering+ Applications*], International Society for Optics and Photonics (2014).
- [7] Prigozhin, G. Y., Kissel, S. E., Bautz, M. W., Grant, C., LaMarr, B., Foster, R. F., Ricker, G. R., and Garmire, G. P., “Radiation damage in the Chandra x-ray CCDs,” in [*X-Ray Optics, Instruments, and Missions III*], Truemper, J. E. and Aschenbach, B., eds., *Society of Photo-Optical Instrumentation Engineers (SPIE) Conference Series* **4012**, 720–730 (July 2000).
- [8] Caroli, E., Stephen, J. B., Di Cocco, G., Natalucci, L., and Spizzichino, A., “Coded aperture imaging in X- and gamma-ray astronomy,” *Space Science Reviews* **45**, 349–403 (Sept. 1987).
- [9] Nittler, L. R., McCoy, T. J., Clark, P. E., Murphy, M. E., Trombka, J. I., and Jarosewich, E., “Bulk element compositions of meteorites: A guide for interpreting remote-sensing geochemical measurements of planets and asteroids,” *Antarctic Meteorite Research* **17**, 231 (2004).
- [10] Thompson, A. C. and Vaughan, D., eds., [*X-ray Data Booklet*], Lawrence Berkeley National Laboratory, University of California, second ed. (Jan. 2001).
- [11] Jenkins, R., [*Quantitative X-ray Spectrometry*], CRC Press (1995).
- [12] Elam, W., Ravel, B., and Sieber, J., “A new atomic database for X-ray spectroscopic calculations,” *Radiation Physics and Chemistry* **63**(2), 121–128 (2002).
- [13] Kissel, L., “RTAB: the Rayleigh scattering database,” (2000).
- [14] Lim, L. F. and Nittler, L. R., “Elemental composition of 433 Eros: New calibration of the NEAR-Shoemaker XRS data,” *Icarus* **200**(1), 129–146 (2009).
- [15] Dere, K., Landi, E., Mason, H., Monsignori Fossi, B., and Young, P., “CHIANTI-an atomic database for emission lines,” *Astronomy and Astrophysics Supplement Series* **125**, 149–173 (1997).
- [16] Landi, E., Young, P., Dere, K., Del Zanna, G., and Mason, H., “CHIANTI-An Atomic Database for Emission Lines. XIII. Soft X-Ray Improvements and Other Changes,” *The Astrophysical Journal* **763**(2), 86 (2013).

- [17] Freeland, S. and Handy, B., “Data analysis with the SolarSoft system,” *Solar Physics* **182**(2), 497–500 (1998).
- [18] Dupree, A. K., Huher, M. C. E., Noyes, R. W., Parkinson, W. H., Reeves, E. M., and Withbroe, G. L., “The Extreme-Ultraviolet Spectrum of a Solar Active Region,” *Astrophysical Journal* **182**, 321–334 (May 1973).
- [19] Meyer, J.-P., “Solar-stellar outer atmospheres and energetic particles, and galactic cosmic rays,” *The Astrophysical Journal Supplement Series* **57**, 173–204 (1985).
- [20] Anders, E. and Grevesse, N., “Abundances of the elements: Meteoritic and solar,” *Geochimica et Cosmochimica acta* **53**(1), 197–214 (1989).
- [21] Golub, L. and Pasachoff, J., [*The Solar Corona*], Cambridge University Press (1997).
- [22] Landi, E. and Drago, F. C., “The quiet-Sun differential emission measure from radio and UV measurements,” *The Astrophysical Journal* **675**(2), 1629 (2008).
- [23] Lumb, D., Warwick, R., Page, M., and De Luca, A., “X-ray background measurements with XMM-Newton EPIC,” *arXiv preprint astro-ph/0204147* (2002).
- [24] Mewe, R., Gronenschild, E., and Van Den Oord, G., “Calculated X-radiation from optically thin plasmas. V,” *Astronomy and Astrophysics Supplement Series* **62**, 197–254 (1985).
- [25] Zombeck, M., [*Handbook of Space Astronomy and Astrophysics*], vol. 104, Cambridge University Press Cambridge (1990).
- [26] Chandra X-ray Center, Chandra Project Science MSFC, and Chandra IPI Teams, “ACIS: Advanced CCD Imaging Spectrometer,” (January 2014). <http://cxc.harvard.edu/proposer/POG/html/chap6.html>.
- [27] Koyama, K., Tsunemi, H., Dotani, T., Bautz, M. W., Hayashida, K., Tsuru, T. G., Matsumoto, H., Ogawara, Y., Ricker, G. R., Doty, J., et al., “X-ray imaging spectrometer (XIS) on board Suzaku,” *Publications of the Astronomical Society of Japan* **59**(sp1), S23–S33 (2007).
- [28] Hubbell, J. H. and Seltzer, S. M., “Tables of x-ray mass attenuation coefficients and mass energy-absorption coefficients,” *National Institute of Standards and Technology* (1996).
- [29] Ryu, K. K., Burke, B. E., Clark, H. R., Lambert, R. D., O’Brien, P., Suntharalingam, V., Ward, C. M., Warner, K., Bautz, M. W., Binzel, R. P., et al., “Development of CCDs for REXIS on OSIRIS-REx,” in [*SPIE Astronomical Telescopes+ Instrumentation*], 914440–914440, International Society for Optics and Photonics (2014).
- [30] AMPTEK, “XR-100SDD Silicon Drift Detector (SDD),” (February 2014). <http://www.amptek.com/products/xr-100sdd-silicon-drift-detector>.
- [31] Koyama, K., Tsunemi, H., Dotani, T., Bautz, M. W., Hayashida, K., Tsuru, T. G., Matsumoto, H., Ogawara, Y., Ricker, G. R., Doty, J., Kissel, S. E., Foster, R., Nakajima, H., Yamaguchi, H., Mori, H., Sakano, M., Hamaguchi, K., Nishiuchi, M., Miyata, E., Torii, K., Namiki, M., Katsuda, S., Matsuura, D., Miyauchi, T., Anabuki, N., Tawa, N., Ozaki, M., Murakami, H., Maeda, Y., Ichikawa, Y., Prigozhin, G. Y., Boughan, E. A., Lamarr, B., Miller, E. D., Burke, B. E., Gregory, J. A., Pillsbury, A., Bamba, A., Hiraga, J. S., Senda, A., Katayama, H., Kitamoto, S., Tsujimoto, M., Kohmura, T., Tsuboi, Y., and Awaki, H., “X-Ray Imaging Spectrometer (XIS) on Board Suzaku,” *Publications of the Astronomical Society of Japan* **59**, 23–33 (Jan. 2007).
- [32] Lodders, K. and Fegley, B., [*The Planetary Scientist’s Companion*] (1998).

- [33] Nolan, M., Magri, C., Howell, E., Benner, L., Giorgini, J., Hergenrother, C., Hudson, R., Lauretta, D., Margot, J., Ostro, S., and Scheeres, D., “Asteroid (101955) Bennu Shape Model V1.0. EAR-A-I0037-5-BENNUSHAPE-V1.0,” (2013). NASA Planetary Data System.
- [34] Inamdar, N. K., “Radiation Damage for REXIS CCDs,” REXIS internal whitepaper (2013).
- [35] Bralower, H., *Mechanical design, calibration, and environmental protection of the REXIS DAM*, Master’s thesis, Massachusetts Institute of Technology (2013).
- [36] Agostinelli, S., Allison, J., Amako, K. a., Apostolakis, J., Araujo, H., Arce, P., Asai, M., Axen, D., Banerjee, S., Barrand, G., et al., “GEANT4 a simulation toolkit,” *Nuclear instruments and methods in physics research section A: Accelerators, Spectrometers, Detectors and Associated Equipment* **506**(3), 250–303 (2003).